2011-12

Properties and applications of lossy metamaterials

Doumenis, Christos

Monterey, California. Naval Postgraduate School

NAVAL POSTGRADUATE SCHOOL

MONTEREY, CALIFORNIA

THESIS

PROPERTIES AND APPLICATIONS OF LOSSY METAMATERIALS

by

Christos Doumenis

December 2011

Thesis Co-Advisors: David Jenn
James Luscombe
Brett Borden

Approved for public release; distribution is unlimited

THIS PAGE INTENTIONALLY LEFT BLANK

REPORT DOCUMENTATION PAGE			Form Approved OMB No. 0704-0188
Public reporting burden for this collection of information is estimated to average 1 hour per response, including the time for reviewing instruction, searching existing data sources, gathering and maintaining the data needed, and completing and reviewing the collection of information. Send comments regarding this burden estimate or any other aspect of this collection of information, including suggestions for reducing this burden, to Washington headquarters Services, Directorate for Information Operations and Reports, 1215 Jefferson Davis Highway, Suite 1204, Arlington, VA 22202-4302, and to the Office of Management and Budget, Paperwork Reduction Project (0704-0188) Washington DC 20503.			
1. AGENCY USE ONLY ***(Leave blank)***	**2. REPORT DATE** December 2011	**3. REPORT TYPE AND DATES COVERED** Master's Thesis	
4. TITLE AND SUBTITLE Properties and Applications of Lossy Metamaterials		**5. FUNDING NUMBERS**	
6. AUTHOR(S) Christos Doumenis			
7. PERFORMING ORGANIZATION NAME(S) AND ADDRESS(ES) Naval Postgraduate School Monterey, CA 93943-5000		**8. PERFORMING ORGANIZATION REPORT NUMBER**	
9. SPONSORING /MONITORING AGENCY NAME(S) AND ADDRESS(ES) N/A		**10. SPONSORING/MONITORING AGENCY REPORT NUMBER**	
11. SUPPLEMENTARY NOTES The views expressed in this thesis are those of the author and do not reflect the official policy or position of the Department of Defense or the U.S. Government. IRB Protocol number _____N/A_____.			
12a. DISTRIBUTION / AVAILABILITY STATEMENT Approved for public release; distribution is unlimited		**12b. DISTRIBUTION CODE** A	

13. ABSTRACT (maximum 200 words)

The complex permittivity (ε) and permeability (μ) of a material determines the response of the material to electromagnetic radiation. In many cases, the real part of ε and μ are both positive for materials that can be found in nature. Metamaterials (MTMs) are engineered media that are designed to have either a negative permittivity or a negative permeability or both. Negative permittivity and permeability cause electromagnetic waves travelling through this medium to exhibit unusual characteristics.

The zero specular reflection layers using double negative (DNG) materials were examined in the first part of this thesis. The equations related to specular absorbers are analyzed based on the transmission line approach and numerical solutions are used in order to generate universal design charts for zero specular reflection absorbers. A MATLAB program is developed in order to generate the universal curves for double-positive (DPS) and DNG materials.

Several methods to extract the effective permittivity and permeability of both normal materials and MTMs from measured or simulated scattering parameters were examined in the second part of this thesis. Microwave Studio (MWS) by Computer Simulation Technology (CST) was used to model the materials in a free space environment in order to calculate the S-parameters (S_{11} and S_{21}) from which the constitutive parameters μ and ε can be extracted. The results were compared to published data.

14. SUBJECT TERMS Metamaterials, Negative Index, Universal Design Chart, Transcendental Equation, Complex Permittivity and Permeability, Constitutive Parameters, S-parameters			**15. NUMBER OF PAGES** 97
			16. PRICE CODE
17. SECURITY CLASSIFICATION OF REPORT Unclassified	**18. SECURITY CLASSIFICATION OF THIS PAGE** Unclassified	**19. SECURITY CLASSIFICATION OF ABSTRACT** Unclassified	**20. LIMITATION OF ABSTRACT** UU

NSN 7540-01-280-5500 Standard Form 298 (Rev. 2-89)
Prescribed by ANSI Std. 239-18

THIS PAGE INTENTIONALLY LEFT BLANK

Approved for public release; distribution is unlimited

PROPERTIES AND APPLICATIONS OF LOSSY METAMATERIALS

Christos Doumenis
Lieutenant Junior Grade, Hellenic Navy
B.S., Hellenic Naval Academy, 2004

Submitted in partial fulfillment of the
requirements for the degrees of

MASTER OF SCIENCE IN APPLIED PHYSICS
and
MASTER OF SCIENCE IN ELECTRICAL ENGINEERING

from the

NAVAL POSTGRADUATE SCHOOL
December 2011

Author: Christos Doumenis

Approved by: David Jenn
Thesis Co-Advisor

James Luscombe
Thesis Co-Advisor

Brett Borden
Thesis Co-Advisor

Andres Larraza
Chair, Department of Physics

R. Clark Robertson
Chair, Department of Electrical and Computer Engineering

THIS PAGE INTENTIONALLY LEFT BLANK

ABSTRACT

The complex permittivity (ε) and permeability (μ) of a material determines the response of the material to electromagnetic radiation. In many cases, the real part of ε and μ are both positive for materials that can be found in nature. Metamaterials (MTMs) are engineered media that are designed to have either a negative permittivity or a negative permeability or both. Negative permittivity and permeability cause electromagnetic waves travelling through this medium to exhibit unusual characteristics.

The zero specular reflection layers using double negative (DNG) materials were examined in the first part of this thesis. The equations related to specular absorbers are analyzed based on the transmission line approach and numerical solutions are used in order to generate universal design charts for zero specular reflection absorbers. A MATLAB program is developed in order to generate the universal curves for double-positive (DPS) and DNG materials.

Several methods to extract the effective permittivity and permeability of both normal materials and MTMs from measured or simulated scattering parameters were examined in the second part of this thesis. Microwave Studio (MWS) by Computer Simulation Technology (CST) was used to model the materials in a free space environment in order to calculate the S-parameters (S_{11} and S_{21}) from which the constitutive parameters μ and ε can be extracted. The results were compared to published data.

THIS PAGE INTENTIONALLY LEFT BLANK

TABLE OF CONTENTS

LIST OF FIGURES

LIST OF TABLES

THIS PAGE INTENTIONALLY LEFT BLANK

LIST OF ACRONYMS AND ABBREVIATIONS

MTM	Metamaterials
DPS	Double-Positive
DNG	Double-Negative
CST	Computer Simulation Technology
MWS	Microwave Studio
RAM	Radar Absorbing Material
RH	Right-Handed
LH	Left-Handed
PEC	Perfect Electric Conductor
EM	Electromagnetic
RCS	Radar Cross Section
FDTD	Finite Difference Time Domain
SRR	Split-Ring Resonator
CPR	Coplanar Ring
ENG	Epsilon-Negative
MNG	Mu-Negative
SNG	Single-Negative
NRI	Negative Refractive Index
FIT	Finite Integration Technique

THIS PAGE INTENTIONALLY LEFT BLANK

EXECUTIVE SUMMARY

In recent years, there has been an increasing interest in the research and the development of new materials with characteristics that may not be found in nature. Examples of these materials are metamaterials (MTMs), left-handed (LH) media and negative–index materials (NIM). They have many applications not only in scientific areas but also in industrial areas. Some examples of these applications include artificial dielectrics, lens, absorbers, antenna structures, optical and microwave components, frequency-selective surfaces, and composite materials. In this thesis, we examine lossy MTMs and their use as a radar absorbing material (RAM).

First, an analysis of the basic characteristics of MTMs is presented and the properties of MTMs are discussed. A classification of lossy MTM depending on the sign of index of refraction and the signs of the complex permittivity $\varepsilon_r = \varepsilon_r' - j\varepsilon_r''$ and permeability $\mu_r = \mu_r' - j\mu_r''$ is defined in terms of $A = \varepsilon_r'\mu_r' - \varepsilon_r''\mu_r''$ and $B = \varepsilon_r'\mu_r'' + \varepsilon_r''\mu_r'$ parameters. A classification of double positive (DPS), double negative (DNG) and single negative (SNG) materials with the triads of RH and LH is visualized by using the axis of A and B. When $B < 0$, both the phase constant β and the refractive index n are negative, and when $B > 0$ the phase constant and the refractive index are both positive. The parameter A is negative in SNG materials but can be positive or negative in DPS and ENG materials.

Next, an analysis of zero specular absorbers is presented. The equations related to specular absorbers are derived based on transmission line theory. Numerical solutions of the equations are used to generate the universal design curves for zero specular reflection layers, and a solution of a transcendental equation is given for a perfect electric conductor (PEC) backing. Furthermore, a solution for the transcendental equations for both DPS and DNG layers is programmed in MATLAB in order to examine the solutions for the layer parameters. A comparison between DPS and DNG solutions reveals a symmetry

between DPS and DNG layers. From the final versions for the transcendental equations for DPS and DNG layers, we can conclude that the DNG solutions are the complex conjugate of DPS solutions.

Finally, a retrieval program is used to extract the permittivity and permeability of MTM models that were simulated in Microwave Studio (MWS). A brief summary of the relationship between the S-parameters in the free space environment and μ and ε is given. These equations were programmed in MATLAB. Different types of materials, including "normal" materials and MTMs, are simulated in MWS, and the results are exported to the MATLAB program in order to extract the real and the imaginary parts of the permittivity, permeability, index of refraction and impedance. Also, a calculation of the resonant frequency, the frequency in which the effective permeability becomes negative and the left-handed behavior becomes evident, is given. A comparison between the simulation data and the published data is presented.

The results using simulated scattering parameters were in good agreement with available published data when electric and magnetic boundaries were used in MWS. Agreement was not good when using unit cell boundaries and Floquet modes. This discrepancy is likely due to the form of the Floquet mode fields and how they are converted to scattering parameters data for use in the MATLAB script. This should be investigated further in subsequent research.

ACKNOWLEDGMENTS

I would like to thank to my beloved country, Greece, and the Hellenic Navy for offering me the opportunity to study and to enhance my academic horizons at the Naval Postgraduate School.

I would like to express my most sincere gratitude to Professor David C. Jenn, Naval Postgraduate School, Monterey, California, for his guidance and suggestions in the completion of this work. I would also like to thank Professor James Luscombe and Professor Brett Borden for agreeing to be the second readers for this thesis, and for their support to explaining the theoretical background of this thesis. Each of them prepared me in electromagnetism and radar cross section theory, which formed a basis for my thesis work.

I would like to thank to my parents, Ioannis and Eleftheria, my sister, Evangelia, and her husband, Charalambos, for their endless support and understanding, and especially to my sister who always tried to teach me the real values of life.

Finally, I would like to thank to my lovely wife, Anastasia, for everything she did for me. I must acknowledge the constant and unconditional support that I received throughout this project from her and without whom this work could have never been completed. Furthermore, this work is totally dedicated to our baby boy, Ioannis Doumenis, for the happiness which he brought to us at 18 August 2011 and to my father Ioannis, who won the battle with an incurable disease, and now is more healthy than ever.

THIS PAGE INTENTIONALLY LEFT BLANK

I. INTRODUCTION

A. OVERVIEW

In the frequency domain, all materials can be described electrically by their complex permittivity (ε) and permeability (μ). These two basic parameters determine the response of the material to electromagnetic (EM) radiation. In most cases, the real parts of ε and μ are both positive for materials that can be found in nature. While some materials can have negative ε, materials having negative μ are less common than negative-ε-materials, including ferromagnetic and antiferromagnetic resonant systems [1]. Over 30 years ago, the Russian physicist Victor Veselago postulated the existence of a material in which both the permittivity and permeability were assumed to have negative, real values (negative index of refraction). They are called double-negative (DNG) materials.

Metamaterials (MTMs) is a general term for artificial media that are designed to have either a negative permittivity or permeability, or both. The term derives from the Greek word *meta*, meaning beyond. According to [2], "MTMs *are macroscopic composites having man-made, three dimensional, periodic cellular architecture designed to produce an optimized combination, not available in nature, of two or more responses to specific excitation*." The dimensions of these cells are usually much smaller than the operating wavelength. In this case, the medium can be considered homogeneous, and it is feasible to define effective (macroscopic) constitutive parameters.

Negative permittivity and permeability cause electromagnetic waves travelling through the medium to exhibit unusual characteristics. Moreover, due to the negative index of refraction, the phase fronts and the group velocity (power flow) of an electromagnetic wave are in opposite directions and have a left-hand sense. Therefore, they are referred to as left-handed (LH) materials. These properties may be used in many applications, such as novel shapes and sizes for antennas and lenses as well as constraining or expanding their bandwidth.

In this thesis, an analysis of the basic parameters of MTMs is presented along with their unusual characteristics and the differences from "normal" materials. One potential application is radar cross section (RCS) reduction. MTMs used in radar absorbing material (RAM) layers may have some advantage over conventional material. We analyze the matched surface impedance RAM and zero specular reflection absorbers. The equations related to specular absorbers are analyzed from a MTMs approach. Numerical methods for solving the transcendental equations and presentation of the results in the form of a universal design chart for MTMs are given. In particular, the effects of electric and magnetic losses are considered. In addition, some MTM configurations are simulated using the numerical simulation computer program Microwave Studio (MWS) by Computer Simulation Technology (CST). The data are generated in preparation for assisting in the validation of a new finite-difference time-domain (FDTD) code that will be capable of analyzing nonlinear effects in MTMs.

B. LITERATURE REVIEW

MTMs are a class of effectively homogeneous, artificial materials not found in nature. In [3], Veselago demonstrated that a DNG medium results in unusual optical phenomena when light passed through it. One property was that the phase front propagated in the opposite direction than in a normal medium (so-called right-hand media). Thus, DNG materials are also called left-handed media.

In [4], Pendry proposed a MTM based on the split-ring resonator (SRR), which is a subwavelength structure consisting of two planar concentric rings facing in opposite directions. SRRs were first demonstrated at gigahertz frequencies by Smith [5] and Shelby [6]. The SRR were combined with copper wires embedded in a fiber glass circuit board. Conductive copper provided the negative electric permittivity, while the SRR itself increased the magnetic response of the material. An example is shown in Figure 1. In this example the SRRs are conducting squares.

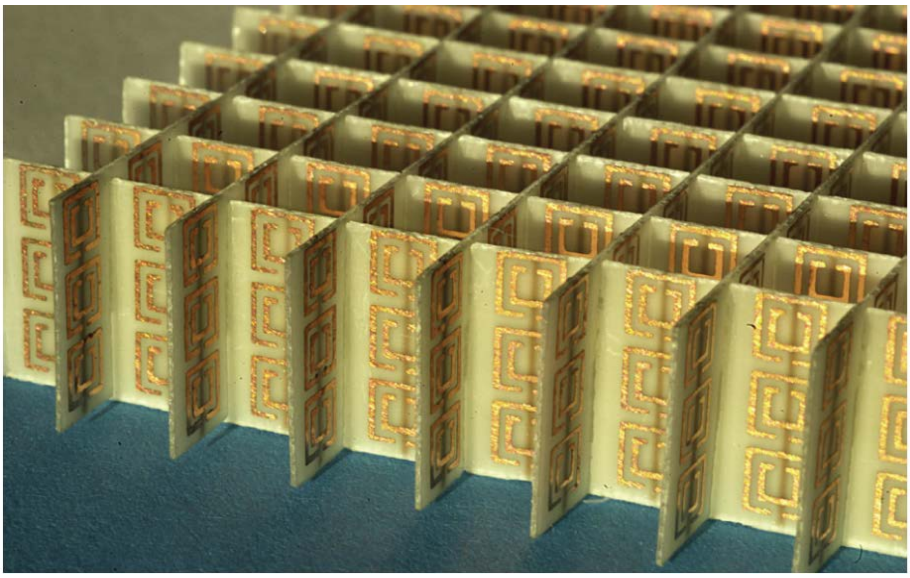

Figure 1. A negative index MTM formed by SRRs and wires deposited on opposite sides of a standard circuit board (From [7]).

In [8], a group at MIT proposed a method to use photonic crystals to produce negative refraction while at the same time maintaining a positive group velocity and a positive refractive index. In [9], a research group lead by Anthony Hoffman produced the first semi-conductor-based MTM exhibiting negative refraction at optical frequencies. Since the 1990s, a vast amount of research has been conducted on MTMs and their applications. Numerous conferences and books have been devoted to the topic [2], [3], [4], [6].

C. THESIS OBJECTIVE

The objective of this thesis is to consider the performance characteristics of lossy MTMs and how they might be used in a matched surface RAM technique. Universal design charts based on the MTMs are presented. Numerical simulations are used to study the properties of lossy MTMs and examine whether they could be used to advantage as a RAM. A universal chart for DNG materials is constructed, and its relationship for the chart for DPS materials is noted.

MWS is used to model the materials and calculate the S-parameters for comparison purposes. The ε and μ extraction calculation is done with a MATLAB program. To validate the program, test cases are presented and simulation results are compared to published data.

D. THESIS OUTLINE

The thesis is organized as follows. The topic was introduced and the importance of the research outlined in Chapter I. The necessary background is developed in order to understand the interaction of waves with MTMs in Chapter II. In Chapter III, the analysis of matched wave impedance RAM and zero specular reflection absorbers are discussed. The equations relating to specular absorbers are extended to MTMs numerical methods for solving the resulting transcendental equations, and presentation of the results in the form of a universal design chart for MTMs are given. In Chapter IV, the free space environment retrieval method is discussed. The simulation setup using MWS for the free space environment is presented. The results extracted from the S-parameters are compared with published data. Finally, in Chapter V, the results, conclusions and suggestions for future studies are discussed.

II. METAMATERIALS

The basic background theory for the behavior of waves in DNG materials is provided in this chapter in order to understand the analysis presented in later chapters.

A. INTRODUCTION

MTMs are broadly defined as artificial, effectively homogeneous materials possessing unusual electromagnetic properties not found in nature [10]. The history of MTMs can be tracked back to 1968 when Russian physicist Victor Veselago published his now-famous paper [3] and posed the question "What would happen if a material had both negative permittivity and permeability?" His most striking conclusion was that a negative sign must be chosen for the index of refraction of a DNG material [2]. In other words, for a lossless medium

$$n = -\sqrt{\mu\varepsilon} \tag{2.1}$$

where μ and ε are positive.

This observation lead Veselago to design specific MTMs, and he demonstrated an unusual optical phenomena when light passes through them. That is, the wave front propagates in a direction opposite the power flow. Victor Veselago's prediction was verified after more than 30 years, when John Pendry (Imperial College, London) showed how these materials could be created artificially [4], [11], [12]. Then, in the following year, he published a paper in which he proposed that MTMs be used to make a perfect lens [12]. In the same year (2000), a University of California San Diego group demonstrated the first left-handed material [13], [14]. This group started a field of structured materials to create electromagnetic response not available in naturally occurring materials [15]. Their material made use of an array of conducting, nonmagmetic, ring-shaped local resonator elements and an array of conducting continuous wires, shown in Figure 1 of Chapter I, in order to achieve negative permeability and permittivity.

B. NEGATIVE PERMITTIVITY AND PERMEABILITY

In a source free and lossy medium, Maxwell's equations in phasor form for a $e^{j\omega t}$ time convention are:

$$\nabla \times \vec{E} = -j\omega\mu\vec{H} \tag{2.2}$$

$$\nabla \times \vec{H} = j\omega\varepsilon\vec{E} \tag{2.3}$$

$$\nabla \times \vec{E} = 0 \tag{2.4}$$

$$\nabla \times \vec{H} = 0 \tag{2.5}$$

where $\vec{E}$ (V/m) and $\vec{H}$ (A/m) are the electric and magnetic field intensities. The factors ε and μ are often expressed in terms of the complex relative permittivity ε_r and the complex relative permeability μ_r of the material as

$$\varepsilon = \varepsilon_o\varepsilon_r = \varepsilon_0(\varepsilon_r' - j\varepsilon_r'') \tag{2.6}$$

$$\mu = \mu_o\mu_r = \mu_0(\mu_r' - j\mu_r'') \tag{2.7}$$

where $\varepsilon_o = 8.854\times10^{-12}$ F/m and $\mu_o = 4\pi\times10^{-7}$ H/m are the permittivity and permeability of free space, respectively. The imaginary parts ε_r'' and μ_r'' are due to the losses from electric and magnetic damping and finite conductivity. Note that ε_r'' and μ_r'' must be positive in a passive medium due to the conservation of energy [7].

Generally, materials are categorized with regard to their constitutive parameters σ, μ and ε. The ohmic losses due to finite conductivity σ and polarization due to ε_r'' can be lumped together [6]. In our representation, σ is combined with ε_r''.

Materials can be further classified as linear or nonlinear, conducting or nonconducting, dispersive or nondispersive, homogeneous or inhomogeneous and isotropic, anisotropic or bianisotropic. The generalized representation of matrix constitutive relations that covers all these cases is the Tellegen representation. The fields are related to the flux densities by:

$$\begin{bmatrix} \vec{D} \\ \vec{B} \end{bmatrix} = \begin{pmatrix} \varepsilon & \xi \\ \zeta & \mu \end{pmatrix} \begin{bmatrix} \vec{E} \\ \vec{H} \end{bmatrix} \tag{2.8}$$

where in the Cartesian system the vectors and matrices, respectively, have the forms:

$$\vec{D} = \begin{bmatrix} D_x \\ D_y \\ D_z \end{bmatrix} \tag{2.9}$$

$$\varepsilon = \begin{pmatrix} \varepsilon_{xx} & \varepsilon_{xy} & \varepsilon_{xz} \\ \varepsilon_{yx} & \varepsilon_{yy} & \varepsilon_{yz} \\ \varepsilon_{zx} & \varepsilon_{zy} & \varepsilon_{zz} \end{pmatrix} \tag{2.10}$$

and

$$\mu = \begin{pmatrix} \mu_{xx} & \mu_{xy} & \mu_{xz} \\ \mu_{yx} & \mu_{yy} & \mu_{yz} \\ \mu_{zx} & \mu_{zy} & \mu_{zz} \end{pmatrix} \tag{2.11}$$

where the elements ε_{ij} and μ_{ij} ($i, j = x$, y or z) are the complex relative values that completely describe the permittivity and permeability of the material, respectively [16]. The off-diagonal blocks of the matrix in Equation (2.8) are zero for the material of interest in this study.

Lossless materials where $\varepsilon_r' > 0$ and $\mu_r' > 0$ are referred to as DPS or RH materials because the direction of power flow given by the Poynting vector $\vec{W}$ is, according to right-handed rule,

$$\vec{W} = \vec{E} \times \vec{H}, \tag{2.12}$$

and the propagation vector $\vec{k}$ is in the direction of $\vec{W}$

$$\vec{k} = \hat{k}\kappa_0 \sqrt{\varepsilon_r' \mu_r'} \tag{2.13}$$

where $\kappa_o = \omega\sqrt{\mu_o \varepsilon_o} = \dfrac{2\pi}{\lambda_o}$, λ_o is the free space wavelength and $\omega = 2\pi f$ is the radian frequency.

Now, let us examine the case where both ε_r' and μ_r' are negative. This case is referred to as a DNG material. Then, the direction of propagation for this kind of material is

$$\vec{k} = \hat{k}\kappa_0\sqrt{|\varepsilon_r'||\mu_r'|} = \hat{k}\kappa_o n. \tag{2.14}$$

The wave impedance can be described as [17]:

$$\eta = \eta_o \frac{\sqrt{|\mu_r'|}}{\sqrt{|\varepsilon_r'|}}. \tag{2.15}$$

The different combinations of real permeability and permittivity with multiplying coefficients are listed in Table 1.

Table 1. Multiplicative factor for index of refraction n (After [17]).

n	$\varepsilon_r > 0$	$\varepsilon_r < 0$
$\mu_r > 0$	$+1$	j
$\mu_r < 0$	j	-1

A result of Equation (2.14) is that, for a DNG material, the negative sign flips the angle of refraction in Snell's law, so Snell's law must be amended to

$$\frac{\sin\theta_i}{\sin\theta_t} = \frac{p_2}{p_1}\left|\sqrt{\frac{\mu_{r2}'\varepsilon'_{r2}}{\mu_{r1}'\varepsilon_{r1}'}}\right| \tag{2.16}$$

where p is the "handedness" parameter of a medium given by the determinant

$$p = \begin{pmatrix} \hat{x} \bullet \hat{e} & \hat{y} \bullet \hat{e} & \hat{z} \bullet \hat{e} \\ \hat{x} \bullet \hat{h} & \hat{y} \bullet \hat{h} & \hat{z} \bullet \hat{h} \\ \hat{x} \bullet \hat{k} & \hat{y} \bullet \hat{k} & \hat{z} \bullet \hat{k} \end{pmatrix} \tag{2.17}$$

where $\vec{e} = \vec{E} / \left|\vec{E}\right|$ and $\hat{h} = \vec{H} / \left|\vec{H}\right|$ are unit vectors in the directions of the fields [19].

Based on the equation for the right-handed and left-handed materials, we note the following properties [2] :

1. The field vectors and the direction of phase propagation in DNG material form a left-handed triplet, whereas, in an ordinary medium they are right-handed.
2. The angle of refraction between a DPS medium and a DNG medium are negative.
3. Evanescent waves increase as they propagate through a DNG medium rather than decrease as they do in an ordinary medium.
4. The phase advances in a DNG medium even if lossless and is not retarded as in an ordinary medium.

These properties are discussed further in the following subsections.

1. Left-Hand Rule

All natural materials follow a right-hand rule due to their positive values of relative permeability and permittivity. However, the DNG materials follow the left-hand rule [18], [19]. According to this rule, the flow of energy (Poynting vector), given by

$$\vec{W} = \vec{E} \times \vec{H}, \tag{2.18}$$

is in the opposite direction of the wave front propagation.

2. Negative Index of Refraction

Snell's Law determines the relationship between the angles of incidence and refraction at an interface between two lossless media ($\varepsilon_r = \varepsilon_r'$ and $\mu_r = \mu_r'$) with different indices of refraction

$$n_1 \sin\theta_1 = n_2 \sin\theta_2. \tag{2.19}$$

Thus, the refraction angle θ_2 in Figure 2, would, according to Snell's law, have the same sign as the angle of incidence θ_1 when $n_1 > 0$. In negative-index materials, the index of refraction is negative and, as a result, the refracted wave remains on the same side of the normal as the incident wave. Furthermore, the tangential components of the fields in two media must be equal at the interface regardless of the sign of ε and μ in the two media. The equations for the tangential components are

$$E_{\|1} = E_{\|2} \text{ and } H_{\|1} = H_{\|2}. \tag{2.20}$$

Moreover, the boundary conditions for the normal components imply

$$\varepsilon_1 E_{\perp 1} = \varepsilon_2 E_{\perp 2} \text{ and } \mu_1 H_{\perp 1} = \mu_2 H_{\perp 2} \tag{2.21}$$

$$\vec{k} \times \vec{E} = \frac{\omega}{c} \mu \vec{H} \text{ and } \vec{k} \times \vec{H} = -\frac{\omega}{c} \varepsilon \vec{E}. \tag{2.22}$$

Thus, if ε_1, μ_1 and ε_2, μ_2 have the same signs, the direction of propagation $\vec{k}$ in medium 2 is as indicated at the top in Figure 2 for $n > 0$. However, if ε_2, μ_2 has the sign opposite of ε_1, μ_1, the normal components of $\vec{E}$ and $\vec{H}$ are the opposite of each other according to (2.21), which means that the phase velocity in medium 2 is left-handed [2], as indicated in the bottom of Figure 2.

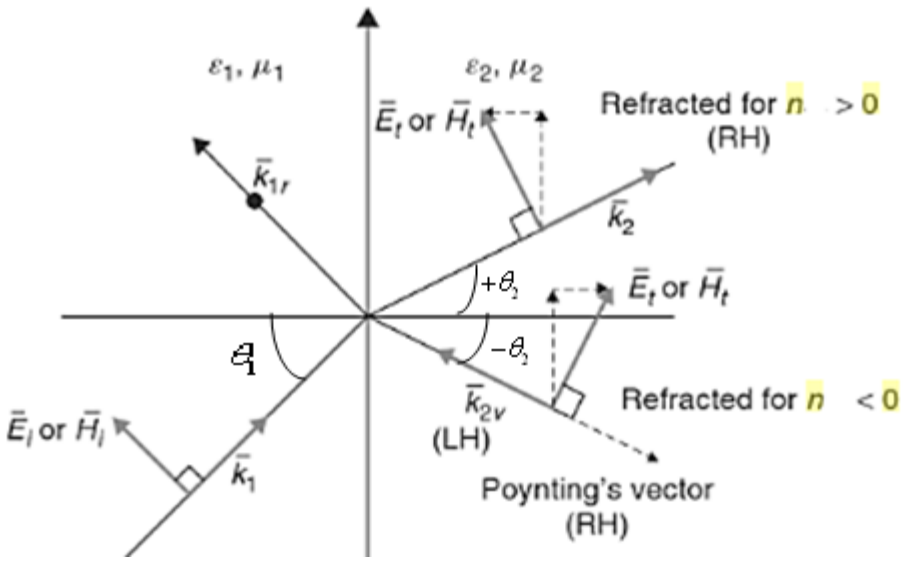

Figure 2. Refraction between a DPS medium 1 and region 2 DPS (top) and DNG (bottom) (After [2]).

The normal component of the electric field changes its direction and so does the normal component of the wave vector. Therefore, the index of refraction must be negative

$$\kappa = \frac{\omega}{c} n \text{ and } n = -\sqrt{\varepsilon_2 \mu_2}. \tag{2.23}$$

With the change of the sign of the refractive index, Snell's law of refraction is modified to [20]

$$\frac{\sin(\theta_1)}{\sin(\theta_2)} = \frac{-\sqrt{\varepsilon_2 \mu_2}}{\sqrt{\varepsilon_1 \mu_1}} = -\frac{n_2}{n_1} \tag{2.24}$$

which is in agreement with Equation (2.16).

3. Evanescent Waves

In Equation (2.1), when $\varepsilon < 0$ and $\mu < 0$, then the index of refraction n is an imaginary number. Due to the fact that n is imaginary, the propagating waves change into evanescent waves [2]. While in a RH medium, the evanescent waves decay exponentially, in LH materials this decay is canceled [5]. Veselago showed that the evanescent waves propagating through this type of medium increase as they move away from their origin [3]

and emerge from the far side of the medium enhanced in amplitude by the transmission process [5]. This does not violate energy conservation because evanescent waves do not carry energy.

4. Phase Advance

If a lossless dielectric slab is placed in front of a ground plane, the input impedance Z_{in} for an ordinary material with $n>0$ is obtained by a phase delay $2\kappa d = 2\kappa_o nd$. Similarly, if $n<0$ there is a phase advance of $2\kappa d$. This motion in both cases has, as a result, a phase delay when $n>0$ and a phase advance when $n<0$ [18, 19]. This property of DNG materials has been used to build electromagnetic "cloaks" that guide waves around objects as shown in Figure 3.

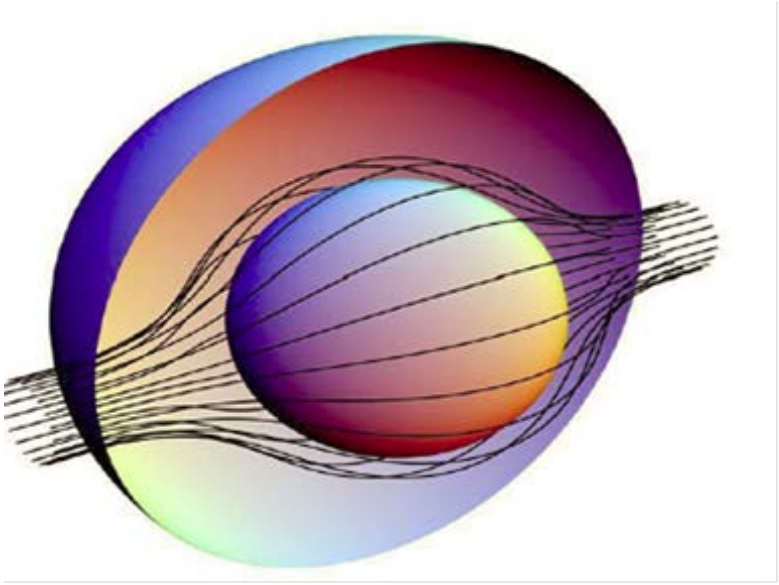

Figure 3. Electromagnetic "Cloak" based on the phase advance property of a DNG (From [20]).

C. REALIZATION OF DNG MATERIALS

Artificial materials are media made of inclusions such that the sizes and spacing of the inclusions are much smaller than the wavelength of incident electromagnetic radiation. This allows a medium to act as an effective bulk medium to electromagnetic waves. Artificial materials can be tailored to produce desired values of the permittivity

and permeability, and have a negative index of refraction at specific frequencies. The applications of this tailoring include electromagnetic cloaking and, theoretically, subwavelength image resolution. They have also been used to improve the performance of antennas and transmission line devices. However, the success of these applications depends on their sensitivity to energy loss.

Artificial materials are a mix of regular materials combined in such a way as to obtain specific and unusual characteristics. For example, negative ε_r' can be obtained using a grid of conducting wires as shown in Figure 4.

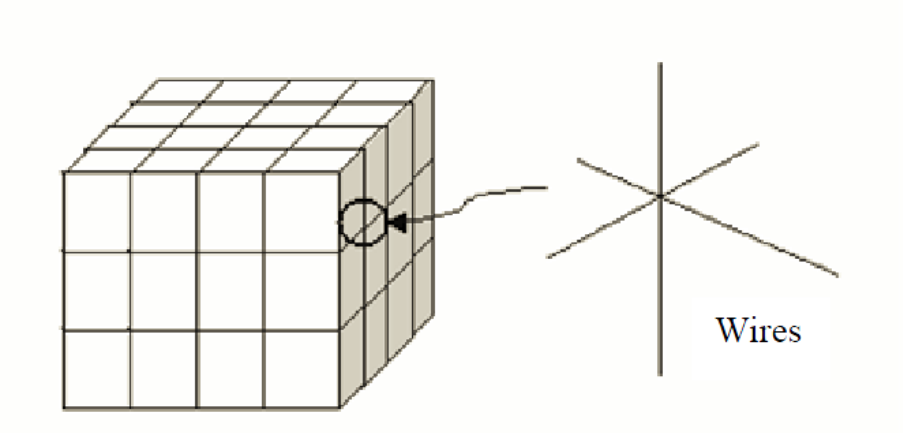

Figure 4. Three-dimensional grid of thin wires approximates a plasma (From [21]).

The effective relative dielectric constant is

$$\varepsilon_{reff} = 1 - \frac{\omega_p^2}{\omega\left(\omega + \frac{j\varepsilon_o a^2 \omega_p^2}{\pi\sigma r^2}\right)} \tag{2.25}$$

where $\omega_p = \frac{2\pi\sigma^2}{a^2 \ln(a/r)}$, r is the radius of the wire, a is the grid spacing and σ is the wire conductivity [22].

A structure that influences both the effective permittivity and permeability is the coplanar ring (CPR). This configuration is shown in Figure 5.

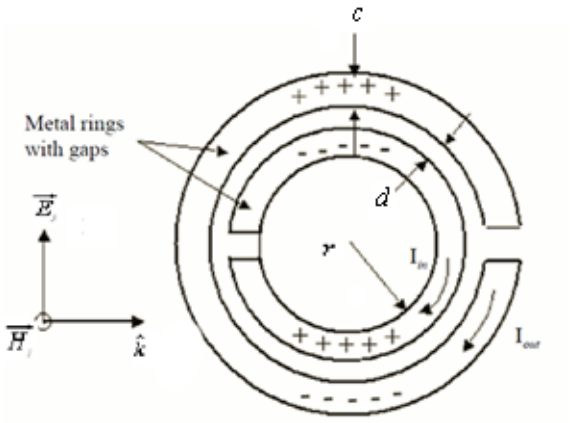

Figure 5. Coplanar ring (After [21]).

According to the Lentz's law, the induced currents oppose the external field and the electric field causes charge separation. Thus, the first effect is a diamagnetic behavior, and the second results in a polarization vector and changing the permittivity. The effective permeability of CPR is given by

$$\mu_{reff} = 1 - \frac{\pi r^2 / a^2}{1 + j\dfrac{2l\rho}{\omega r \mu_o} - \dfrac{3l}{\pi^2 \omega^2 \mu_o C r^3}} \tag{2.26}$$

where ρ is the resistivity of the metal (ohms/m), $C = \dfrac{\varepsilon_o}{\pi} \ln\left(\dfrac{2c}{d}\right)$ is the capacitance per meter of two parallel strips, a the lattice spacing in the plane of rings and l is the spacing between sheets of rings [13], [16].

D. CLASSIFICATION OF MATERIALS

First, we consider lossless materials, where $\varepsilon_r'' = \mu_r'' = 0$. All lossless materials are classified into four types depending on the signs of ε_r' and μ_r', as can be seen in Figure 6. Also labeled in the figure is the plane wave propagation sense: (1) right-handed, RH, or (2) left-handed, LH and (3) evanescent.

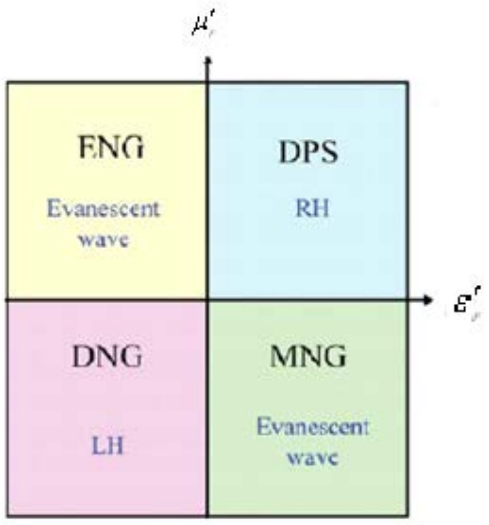

Figure 6. Depiction of ε-μ space for lossless metamaterials (After [10]).

Materials in which $\varepsilon_r' > 0$ and $\mu_r' > 0$ are called double-positive (DPS). In DPS materials the vectors of the electric field, magnetic field, and phase velocity vector form a right-handed triad. Materials in which $\varepsilon_r' < 0$ and $\mu_r' > 0$ are called epsilon-negative (ENG). Periodic wire structures can possess this property [10]. Materials in which $\varepsilon_r' > 0$ and $\mu_r' < 0$ are called mu-negative (MNG). Periodic split-ring resonator (SRR) structures possess this property [11]. In both ENG and MNG materials, the propagation constant is purely real. Therefore, electromagnetic waves become evanescent modes and cannot propagate.

In single-negative (SNG) material, which includes ENG and MNG materials, the vectors of the electric field, magnetic field, and phase velocity vector form a LH triad, so DNG materials are also called LH media. DNG materials have been artificially realized by combining the periodic wire and SRR structures. The index of refraction is negative, so DNG materials are also called negative refractive index (NRI) materials.

Artificially engineered MTMs are always dispersive and lossy because they are resonant structures. Therefore, the classification in Figure 6 is not valid for lossy materials.

At this point, general propagation constant γ is defined for lossy ENG, MNG, and DNG materials. Theoretically, it can been seen how γ is affected by the material constants and by the loss terms of ε and μ. For any material, the propagation constant can be defined as

$$\gamma = \alpha + j\beta = \pm j\omega\sqrt{\varepsilon_r \mu_r} = \pm j\kappa_o \sqrt{\varepsilon_r' \mu_r' - \varepsilon_r'' \mu_r'' - j\left(\varepsilon_r' \mu'' +_r \varepsilon_r'' \mu_r'\right)} \qquad (2.27)$$

where α and β are the attenuation and phase constants, respectively [10]. Note that the $\pm$ sign should be added because β can be either positive or negative. Thus, only the solution that gives a positive α is a real solution because α must be positive due to the conservation of energy. Therefore, the correct sign of β is that which is paired with the positive α.

To simplify Equation (2.27), new parameters that were introduced in [10] are used

$$A = \varepsilon_r' \mu_r' - \varepsilon_r'' \mu_r'' \qquad (2.28)$$

$$B = \varepsilon_r' \mu_r'' + \varepsilon_r'' \mu_r'. \qquad (2.29)$$

A general plot in A-B space is shown in Figure 7. Now we analyze the properties in each region. Much of this discussion is taken from [10].

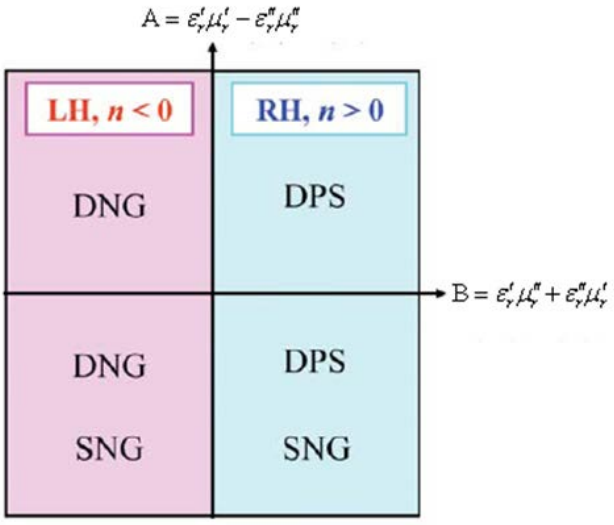

Figure 7. A-B space for lossy metamaterials (After [10]).

Applying Equations (2.28) and (2.29) to Equation (2.27), we get explicit forms of α and β. Thus, for $A \geq 0$, we get

$$\alpha = \pm\kappa_o \left(A^2 + B^2\right)^{1/4} \sin\left(\frac{1}{2}\tan^{-1}\left(\frac{B}{A}\right)\right), \tag{2.30}$$

$$\beta = \pm\kappa_o \left(A^2 + B^2\right)^{1/4} \cos\left(\frac{1}{2}\tan^{-1}\left(\frac{B}{A}\right)\right). \tag{2.31}$$

For $A < 0$, we get

$$\alpha = \pm\kappa_o \left(|A|^2 + B^2\right)^{1/4} \cos\left(\frac{1}{2}\tan^{-1}\left(\frac{B}{|A|}\right)\right), \tag{2.32}$$

$$\beta = \pm\kappa_o \left(|A|^2 + B^2\right)^{1/4} \sin\left(\frac{1}{2}\tan^{-1}\left(\frac{B}{|A|}\right)\right). \tag{2.33}$$

When $\varepsilon_r', \mu_r' > 0$, $\varepsilon_r'' = \mu_r'' = 0$ (lossless DPS: $A > 0$, $B = 0$), $\alpha = 0$ and $\beta = +\kappa_o\sqrt{\varepsilon_r'\mu_r'}$. When $\varepsilon_r' < 0$, $\mu_r' < 0$, $\varepsilon_r'' = \mu_r'' = 0$ (lossless DNG: $A > 0$, $B = 0$), $\alpha = 0$ and $\beta = -\kappa_o\sqrt{|\varepsilon_r'||\mu_r'|}$. In these cases, $\alpha = 0$, so the sign of β can be determined using by consideration of the plane wave propagation in these media [23]. For lossless DPS materials, β is positive, and for lossless DNG materials, β is negative.

For DPS with losses, α and β are expressed by Equations (2.30) and (2.31), respectively, and for DNG with losses, by Equations (2.32) and (2.33), respectively. Note that B for DNG materials is always negative, so that the signs of α and β are opposite. Thus, negative β paired with a positive α is the correct solution for DNG materials. This result confirms that a DNG material operates as an LH triad.

For ENG and MNG without material losses ($A < 0$, $B = 0$), $\alpha = \kappa_o\sqrt{|\varepsilon_r'\mu_r'|}$ and $\beta = 0$. The waves in these materials become evanescent and cannot propagate.

For ENG with electrical losses ($\varepsilon_r' > 0$, $\mu_r' > 0$, $\varepsilon_r'' \neq 0$, $\mu_r'' = 0$), A and B become $\varepsilon_r'\mu_r' < 0$ and $\varepsilon_r''\mu_r' > 0$, respectively, and the sign of $B/|A|$ is positive. Thus,

$$\alpha = +\kappa_o \left(|A|^2 + B^2 \right)^{1/4} \cos\left(\frac{1}{2} \tan^{-1}\left(\frac{\varepsilon_r''}{|\varepsilon_r'|} \right) \right), \tag{2.34}$$

$$\beta = +\kappa_o \left(|A|^2 + B^2 \right)^{1/4} \sin\left(\frac{1}{2} \tan^{-1}\left(\frac{\varepsilon_r''}{|\varepsilon_r'|} \right) \right). \tag{2.35}$$

For this material, $\beta > 0$, which is different from the evanescent case when $\beta = 0$. The wave in this material attenuates exponentially, and β is positive in the wave propagation region. Therefore, this material can be defined as an RH medium.

For ENG with magnetic losses ($\varepsilon_r' < 0, \mu_r' > 0, \varepsilon_r'' = 0, \mu_r'' \neq 0$), A becomes $\varepsilon_r' \mu_r' < 0$ and B becomes $\varepsilon_r' \mu_r'' > 0$, so the sign of $B/|A|$ is negative. Thus, the signs of α and β are opposite:

$$\alpha = +\kappa_o \left(|A|^2 + B^2 \right)^{1/4} \cos\left(\frac{1}{2} \tan^{-1}\left(\frac{\mu_r''}{|\mu_r'|} \right) \right), \tag{2.36}$$

$$\beta = -\kappa_o \left(|A|^2 + \mathrm{B}^2 \right)^{1/4} \sin\left(\frac{1}{2} \tan^{-1}\left(\frac{\mu_r''}{|\mu_r'|} \right) \right). \tag{2.37}$$

The sign of β is negative, so this material is an LH medium. Large attenuation occurs because of the large α as in Equation (2.36). Thus, an ENG material can be either an RH or LH medium depending on the losses of the material.

MNG materials with magnetic losses ($\varepsilon_r' > 0, \mu_r' < 0, \varepsilon_r'' = 0, \mu_r'' \neq 0$) have α and β as expressed by Equations (2.34) and (2.35), respectively. Thus, these materials are RH media. On the other hand, MNG materials with electric loss ($\varepsilon_r' > 0, \mu_r' < 0, \varepsilon_r' \neq 0, \mu_r'' = 0$) have α and β as expressed by Equations (2.36) and (2.37), respectively. Thus, these materials are LH media.

For SNG materials, α and β follow sine and cosine functions, respectively, so only α exists when $B = 0$ or $\varepsilon_r'' = \mu_r'' = 0$, and the values of α and β are similar.

Based on this background, we can classify DPS, ENG and SNG materials with the triads of RH and LH by using the axis of A and B represented in Figure 7. In Figure 7, when $B < 0$, both the propagation constant and the refractive index are negative, and when $B > 0$ the propagation constant and the refractive index are both positive. A is negative in SNG materials but can be positive or negative in DPS and ENG materials.

E. SUMMARY

In this chapter, a brief introduction of metamaterials is given, and their unusual characteristics were discussed. Finally, a classification of lossy materials depending on the signs of ε_r' and μ_r' is defined in terms of two parameters A and B. We classified the different types of metamaterials (DPS, ENG, SNG, DNG) with the triads of RH and LH. In the next chapter these materials are applied to RAM layers.

THIS PAGE INTENTIONALLY LEFT BLANK

III. DESIGN FOR ZERO SPECULAR REFLECTION

A. INTRODUCTION

In this chapter, the analysis of zero specular reflection absorbers is presented. The equations related to specular absorbers are analyzed based on the transmission line theory. Numerical solutions of the equations are used to generate the universal design charts for zero specular reflection layers. Finally, a solution of the transcendental equation for a matched RAM layer over a PEC backing is programmed in MATLAB 7.4 and curves on the universal chart is given for both DPS and DNG layers.

B. EQUATIONS FOR ZERO SPECULAR REFLECTION

Two different conceptual approaches have been applied in the specular reflection reduction application as presented in [24], [25]. The first is the matched-characteristic impedance concept, in which the intrinsic impedance of the material is made equal to the intrinsic impedance of free space. This entails making the relative dielectric constant and relative magnetic permeability of the material equal to each other so there is no front surface reflection from the material. The incident wave is attenuated to a very low amplitude by the round-trip path in an absorption layer that is thick. A layer of such medium placed in front of a conducting plate, the other side of the layer forming a plane interface with free space and illuminated by normally incident plane wave, is shown in Figure 8.

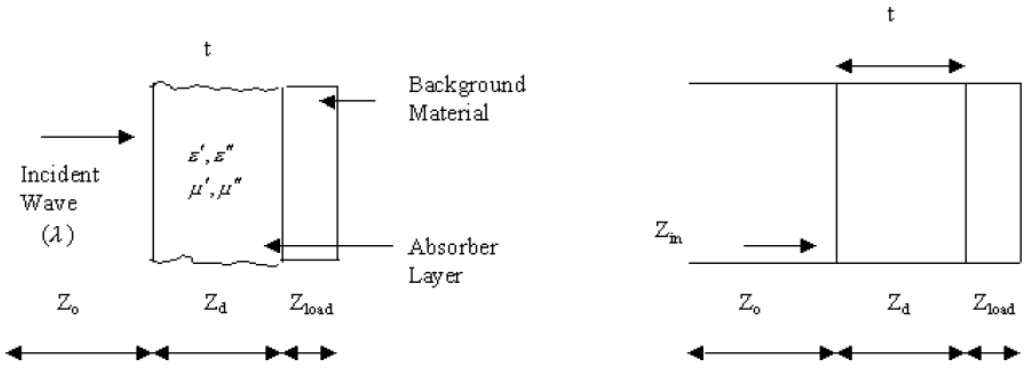

Figure 8. Specular reflection from a coated material and an equivalent transmission line circuit (From [25]).

The second concept is a matched wave impedance approach. The wave impedance is the ratio of total $\vec{E}$ to total $\vec{H}$. The wave impedance at the front surface of the reflector backed material layer is made equal to the intrinsic impedance of free space, thus producing no reflection at all. This approach forms the basis of the studies in this thesis. Referring to Figure 8, we see the six design parameters of wavelength λ, layer thickness t, the real part of the permittivity ε_r', the imaginary part of the permittivity ε_r'', the real part of the permeability μ_r', and the imaginary part of the permeability μ_r''.

A normally incident plane wave having electric field $\vec{E_i}$ and magnetic field $\vec{H_i}$ illuminates the structure. A reflected plane wave having electric field $\vec{E_r}$ and $\vec{H_r}$ results. The electromagnetic field within the absorber layer consists of the sum of forward and backward traveling waves. The wave impedance at any plane parallel to the interface is defined by

$$Z = \frac{\left|\vec{E}_{\tan}\right|}{\left|\vec{H}_{\tan}\right|} \tag{2.38}$$

where $\vec{E}_{\tan}$ is the tangential electric field component and $\vec{H}_{\tan}$ is the tangential magnetic field component. For normal incidence the electric and magnetic field vectors are completely tangential.

The ratio of the reflected wave amplitude to the incident wave amplitude is the reflection coefficient (Γ) defined by

$$\Gamma = \frac{E_{rs}}{E_{is}} \tag{2.39}$$

where the subscript s refers to evaluation at the layer's outer surface. Another more common expression for the reflection coefficient is

$$\Gamma = \frac{Z_{in} - Z_o}{Z_{in} + Z_o} = \frac{Z_{in} / Z_o - 1}{Z_{in} / Z_o + 1} \tag{2.40}$$

where $Z_o = \sqrt{\mu_o / \varepsilon_o}$ [25]. It can been seen from Equation (3.3) that if Z_{in} / Z_o is equal to one, then the reflection coefficient is zero. The impedance at the front surface of the reflector backed material layer is made equal to the intrinsic impedance of free space, thus producing no reflection.

In our case, based on Figure 8, the transmission line equation can be applied for a normally incident wave, so Z_{in} can be defined by

$$Z_{in} = Z_d \frac{Z_L + jZ_d \tan(\gamma t)}{Z_d + jZ_L \tan(\gamma t)} \tag{2.41}$$

where Z_L represents the load presented by the backing material (platform material) and Z_d represents the impedance of the coating layer, where

$$Z_d = \sqrt{\frac{\mu_o(\mu_r' - j\mu_r'')}{\varepsilon_o(\varepsilon_r' - j\varepsilon_r'')}} = Z_o \sqrt{\frac{\mu_r' - j\mu''}{\varepsilon_r' - j\varepsilon_r''}}. \tag{2.42}$$

Note that the propagation constant is complex in this representation

$$\gamma = j\omega\sqrt{\mu\varepsilon} = j\omega\sqrt{\mu_o\mu_r\varepsilon_o\varepsilon_r} = j\kappa_o\sqrt{\left(\mu_r' - j\mu_r''\right)\left(\varepsilon_r' - j\varepsilon_r''\right)}. \tag{2.43}$$

If we normalize each term of Equation (3.3) by Z_o, then Z_{in} / Z_o equal to one is the condition for no reflection for a given Z_L.

C. MATCHING LAYER FOR PEC BACKING

The first step is to find layers that produce zero specular reflection when the background material is set to be PEC ($Z_L = 0$). Thus, Equation (3.4) is simplified to

$$Z_{in} = jZ_d \tan(\gamma t). \tag{2.44}$$

Using the condition for zero specular reflection, we get

$$Z_o = jZ_d \tan(\gamma t). \tag{2.45}$$

Substituting for the constitutive parameters of the medium, we get the transcendental equation

$$j\sqrt{\frac{\mu_r' - j\mu_r''}{\varepsilon_r' - j\varepsilon_r''}}\tan\left[2\pi\left(t/\lambda\right)\sqrt{\left(\mu_r' - j\mu_r''\right)\left(\varepsilon_r' - j\varepsilon_r''\right)}\right] = 1. \tag{2.46}$$

In order to simplify Equation (3.9), the numerator and denominator of the first part of the equation are multiplied by t/λ and rewritten as

$$j\sqrt{\frac{\left(\mu_r' - j\mu_r''\right)\left(t/\lambda\right)}{\left(\varepsilon_r' - j\varepsilon_r''\right)\left(t/\lambda\right)}}\tan\left[2\pi\left(t/\lambda\right)\sqrt{\left(\mu_r' - j\mu''\right)\left(\varepsilon_r' - j\varepsilon''\right)}\right] = 1. \tag{2.47}$$

For convenience a new set of variables can be defined

$$x = \left(t/\lambda\right)\mathrm{Re}[\mu_r] = \left(t/\lambda\right)\mu_r' \tag{2.48}$$

$$y = \left(t/\lambda\right)\mathrm{Im}[\mu_r] = \left(t/\lambda\right)\mu_r'' \tag{2.49}$$

$$a = \left(t/\lambda\right)\mathrm{Re}[\varepsilon_r] = \left(t/\lambda\right)\varepsilon_r' \tag{2.50}$$

$$b = \left(t/\lambda\right)\mathrm{Im}[\varepsilon_r] = \left(t/\lambda\right)\varepsilon_r''. \tag{2.51}$$

Equation (3.10) can be rewritten as

$$j\sqrt{\frac{\left(x - jy\right)}{\left(a - jb\right)}}\tan\left[2\pi\sqrt{\left(x - jy\right)\left(a - jb\right)}\right] = 1. \tag{2.52}$$

The universal chart that depends on six independent parameters that are combined into the four parameter groups in Equations (3.11), (3.12), (3.13) and (3.14) is shown in Figure 9. The last parameter is the dialectic loss tangent $\tan\delta_\varepsilon$, which is given by

$$\tan\delta_\varepsilon = b/a. \tag{2.53}$$

As described in [24], the chart represents combinations of the four parameter groups that result in a zero-reflection absorber with the exception of the lower left region, which is

bounded by $\tan\delta_\varepsilon = 0$. The values of $a = (t/\lambda)\,\mathrm{Re}[\varepsilon_r]$ are read by interpolation between bounding contours of constant values of $b = (t/\lambda)\,\mathrm{Im}[\varepsilon_r]$ (red lines). The values of $\tan\delta_\varepsilon$ are read by interpolation between bounding contours of constant values of $\tan\delta_\varepsilon$ (blue lines). Then it is possible to find the sets of $x = (t/\lambda)\,\mathrm{Re}[\mu_r]$ and $y = (t/\lambda)\,\mathrm{Im}[\mu_r]$, the values of which are read from the abscissa and ordinate scales, respectively.

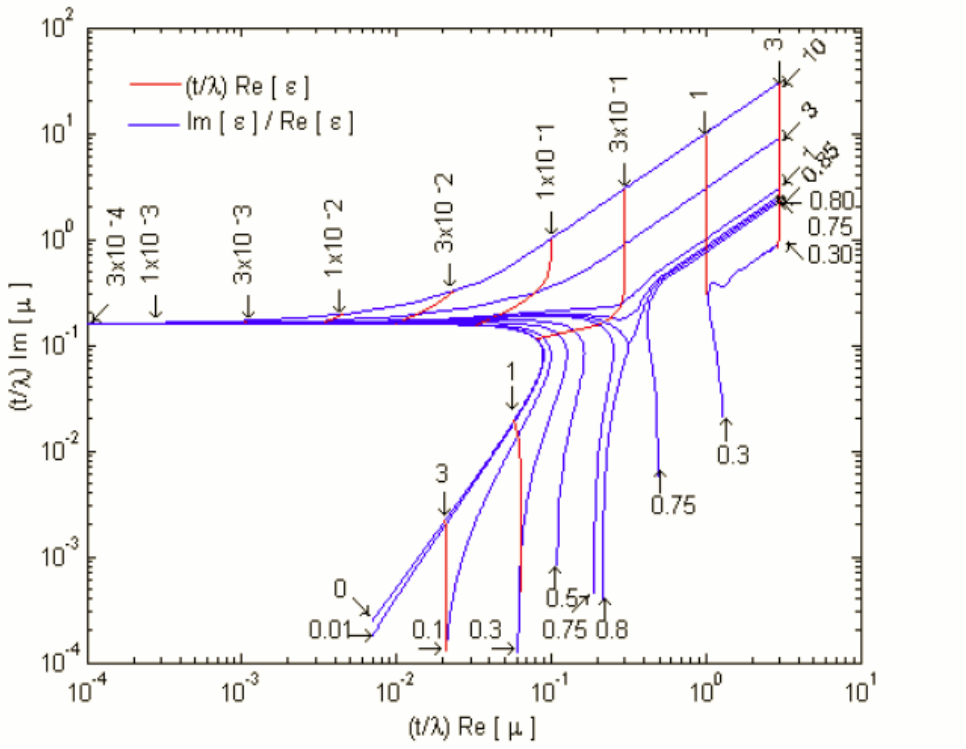

Figure 9. Universal curves for zero specular reflection (From [24]).

As discussed in [24], there are three distinctly different parameter regimes depicted on the chart. The single curve (actually many overlapping curves) at the left side represents thin (less than "quarter-electrical-wavelength" thick) absorbers. Going to the left on this curve requires values of dielectric constant that are less than unity, which is not physically realistic. The region across the top of the chart above the coalesced curve represents the matched characteristic-impedance absorbers. Although, the chart displays contours only for values up to 10, in fact, the entire region progressing from right to left

can be filled with a sequence of similar curves of progressively higher $\tan\delta_\varepsilon$ values. The lower right region of the chart is the location of resonant quarter-electrical-wavelength-thick absorbers [26].

In the region where the dielectric loss tangent is less than 0.3 and $\mathrm{Im}[\mu_r] \geq 3\,\mathrm{Re}[\mu_r]$, the parameters are approximated by

$$\left(2\pi t \big/ \lambda\right)\mathrm{Im}[\mu_r] = 1, \tag{2.54}$$

$$\mathrm{Re}[\varepsilon_r] = 3\,\mathrm{Re}[\mu_r]. \tag{2.55}$$

The required layer thickness in terms of the wavelength and only the imaginary part of the magnetic permeability at that wavelength is determined by Equation (3.17). The relationship between real parts of magnetic permeability and dielectric constant is shown by Equation (3.18). In order to have the reflection close to zero, this equation must be satisfied. The required thickness is also dependent on this equation.

In the upper part of the chart, where $\left(t/\lambda\right)\mathrm{Im}[\mu_r] \geq 1$, the relationship can be defined as

$$\mathrm{Re}[\varepsilon_r] = \mathrm{Re}[\mu_r] \tag{2.56}$$

$$\tan\delta_\varepsilon = \tan\delta_\mu \tag{2.57}$$

where magnetic loss tangent equals to

$$\tan\delta_\mu = \frac{\mathrm{Im}[\mu_r]}{\mathrm{Re}[\mu_r]}. \tag{2.58}$$

Equations (3.19) and (3.20) are equivalent to the statement (complex) that $\varepsilon = \mu$ (real and imaginary part), which is the definition of a matched-characteristic impedance absorber. The intrinsic impedance of the material is equal to the intrinsic impedance of free space. Thus, for all practical purposes, a matched-characteristic impedance absorber is equivalent to a zero reflection absorber when $\left(t/\lambda\right)\mathrm{Im}[\mu_r] \geq 1$.

The lower right region of the chart exhibits a complicated relationship between the parameter groups that constitute a zero-reflection absorber. This region includes the

quarter electrical wavelength thick absorber. The lower part of the chart consists of two subregions. In the left subregion, between $\tan\delta_\varepsilon = 0$ and $\tan\delta_\varepsilon = 0.8$ contours, the thickness of the layer is approximately one-quarter electrical wavelength [24]. It can be expressed as

$$\left(4t/\lambda\right)\mathrm{Re}\left[\left(\mu_r\varepsilon_r\right)^{1/2}\right] \cong 1. \tag{2.59}$$

Equation (3.22) is most accurate near the $\tan\delta_\varepsilon = 0$ contour. Near the bottom of the chart, where dielectric loss dominates, the relationship is $\left(\pi t/\lambda\right)\mathrm{Im}\left(\varepsilon_r\right) \cong 1$.

D. MATCHING LAYERS FOR DPS AND DNG MATERIALS

1. DPS Layers

From Equation (3.15) for a DPS material, x and a are positive; and y and b are zero for a lossless medium and positive for a lossy medium. A sample curve is shown in the form of plot x versus y in the upper left of Figure 10 for fixed values of a and b. This is only one of the many curves that comprise the universal chart in Figure 9. The solution to Equation (3.15) is

$$z = z_1 + jz_2 = x - jy \tag{2.60}$$

which is shown in the upper right of Figure 10. The loss tangent is given in Equation (3.16). The curves were generated using Matlab's *fsolve* function.

The argument in Equation (3.12) is $\gamma t / j$ as we can notice from rewriting Equation (3.15) we get

$$j\sqrt{\frac{x-jy}{a-jb}}\,\tan\underbrace{\left(\pm 2\pi\sqrt{(a-jb)(x-jy)}\right)}_{\gamma t/j} = 1. \tag{2.61}$$

A valid solution for a passive DPS (right-handed) material must have $a, \beta \geq 0$. This is satisfied by selecting the (+) sign in the tangent. A plot of α and β for this case is shown in the lower left of Figure 10.

A plot of the solutions in *A-B* space [10] is shown in the lower right of Figure 10. The parameters *A* and *B* are given in Equations (2.27) and (2.28), respectively. The properties of materials can be classified in terms of these two parameters, with the regions labeled in Figure 7 of Chapter II, Section D. For the example in Figure 10, an *A-B* plot is shown in the lower right.

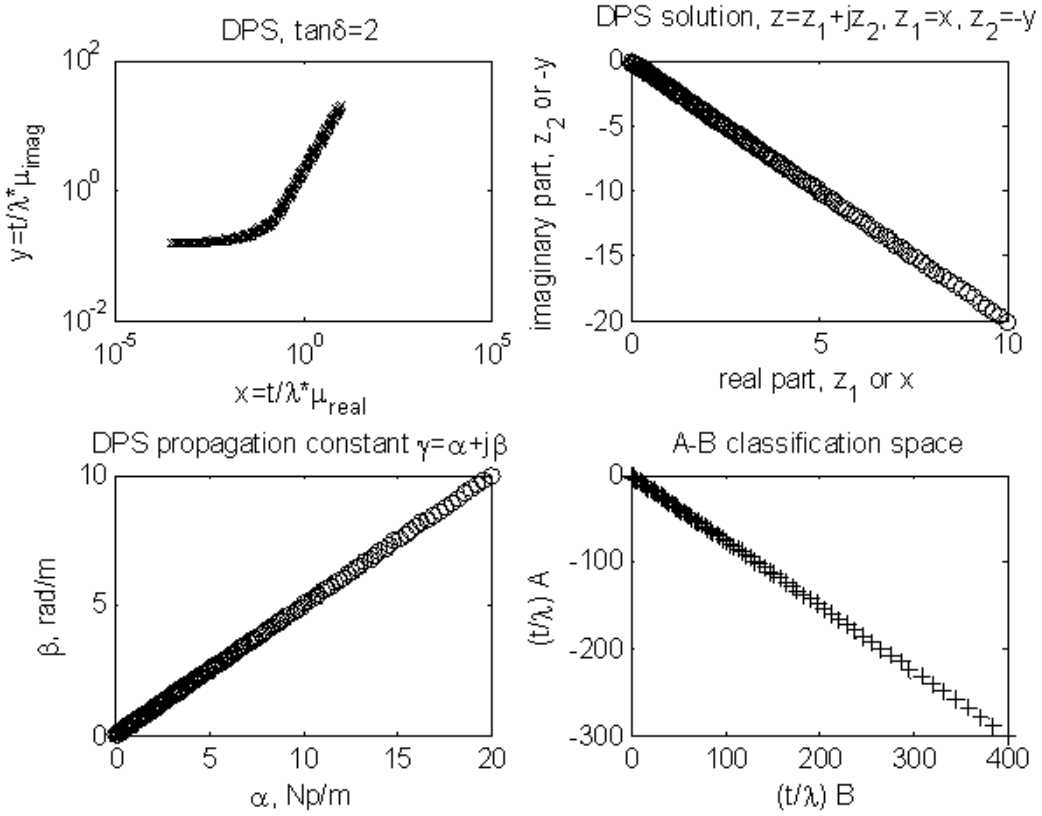

Figure 10. Sample curve solutions for zero specular reflection, DPS materials with $\tan\delta = 2$.

2. DNG Layers

For a DNG material, the real parts of the permittivity and permeability are negative. Therefore, rewriting Equation (3.15) with the negative signs explicitly included, we have

$$j\sqrt{\frac{-x-jy}{-a-jb}}\tan\left(\pm 2\pi\sqrt{(-a-jb)(-x-jy)}\right)=1 \qquad (2.62)$$

whereas before x, y, a and b are all positive. For a DNG (left-handed) material $\alpha \geq 0$ and $\beta < 0$. This is satisfied by selecting the $(-)$ sign in the tangent. Figure 11 is a plot of solutions of Equation (3.25) for $\tan\delta$=2. Note that β is negative as it should be for a DNG material and, in this case, solution points fall in the lower left of $A-B$ space.

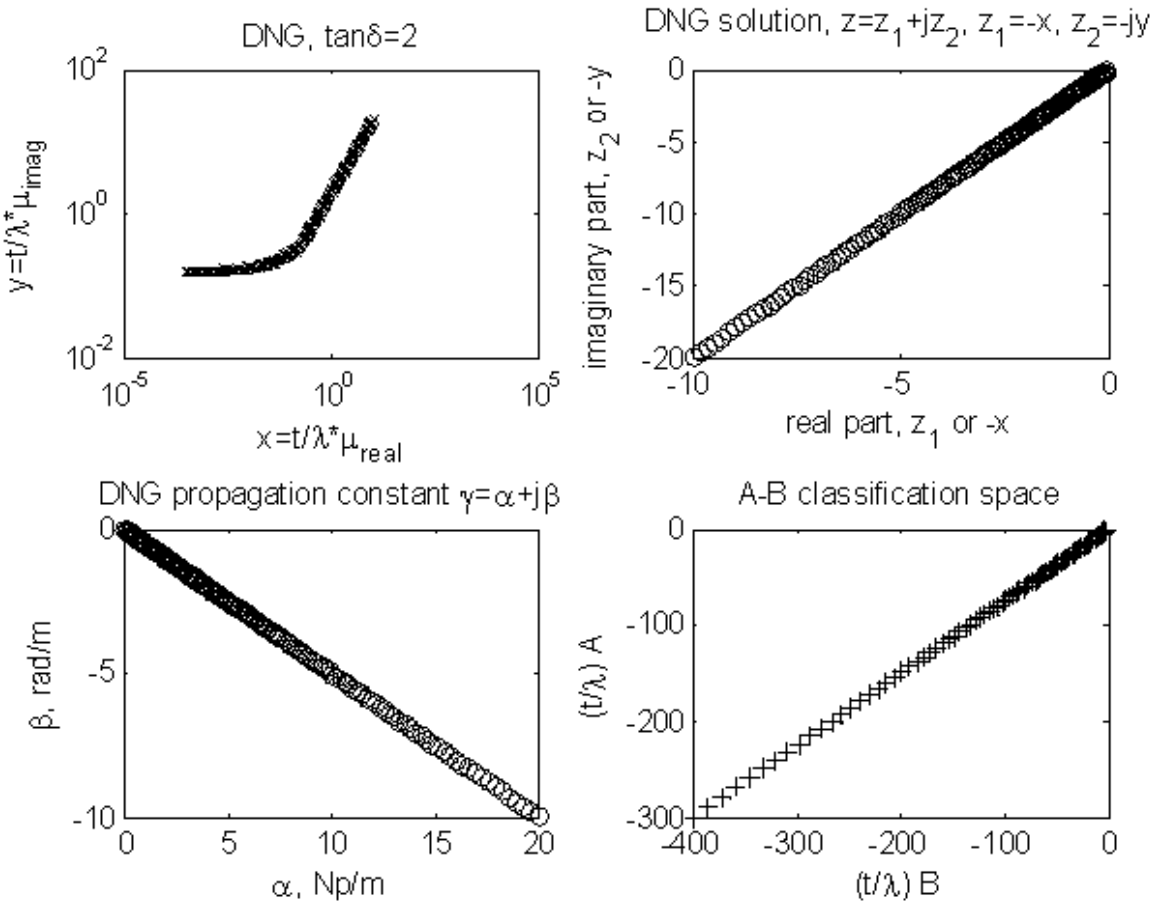

Figure 11. Sample curve solutions for zero specular reflection, DNG materials with $\tan\delta$=2.

E. COMPARISON OF DPS AND DNG LAYERS

In this section, a relationship between DPS and DNG solutions of the transcendental equation is presented in order to recognize the symmetry between Figures 10 and 11.

1. DPS Case

In this case, let the normalized complex permittivity parameter be denoted as $v \equiv a - jb$ and the corresponding solution to Equation (3.25) as $z \equiv x - jy$. In terms of these two quantities, Equation (3.25) can be redefined as

$$j\sqrt{\frac{z}{v}}\tan\left(2\pi\sqrt{zv}\right)=1. \tag{2.63}$$

Using the polar form for the quantities z, z^*, v and v^* (where * denotes complex conjugate), we get

$$z=|z|e^{-j\phi_z},\ -z^*=|z|e^{j\phi_z}\ \text{where}\ \phi_z=\tan^{-1}(y/x), \tag{2.64}$$

and

$$v=|v|e^{-j\phi_v},\ -v^*=|v|e^{j\phi_v}\ \text{where}\ \phi_v=\tan^{-1}(b/a). \tag{2.65}$$

A plot in the complex plane of the quantities z and z^* is shown in Figure12. A similar relationship holds for v and v^*.

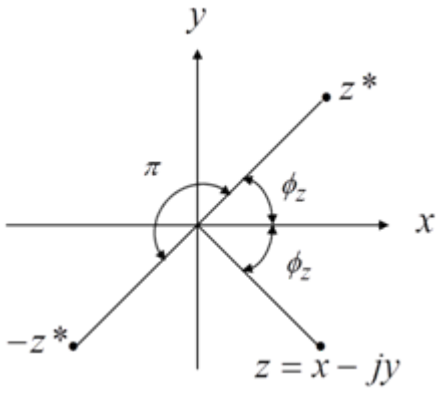

Figure 12. Illustration of the polar form complex parameters z, z^* and $-z^*$.

The product of the square roots of z and v is

$$\sqrt{z\,v}=\sqrt{|z||v|}\,e^{-j\phi_z/2}e^{-j\phi_v/2}=\sqrt{|z||v|}\,e^{-j(\phi_z+\phi_v)/2}. \tag{2.66}$$

So, the solution for a DPS material is

$$\begin{aligned}\alpha + j\beta &= \pm j2\pi\sqrt{vz} \\ &= \pm j2\pi\sqrt{|v||z|}\, e^{-j\Phi} = \pm j2\pi\sqrt{|v||z|}\,(\cos\Phi - j\sin\Phi) \\ &= \pm 2\pi\sqrt{|v||z|}\,(\sin\Phi + j\cos\Phi)\end{aligned} \tag{2.67}$$

where $\Phi \equiv (\phi_z + \phi_v)/2$ and $0 \le \Phi \le \pi/2$. We select in the DPS case the (+) sign so that α and β are positive.

2. DNG Case

Working in the same way as the DPS case, we consider the same value of a and b, namely $-a - jb \equiv -v^*$, where * denotes complex conjugation. Let solutions of Equation (3.25) for a fixed value $-v^*$ be denoted as $-z^*(=-x-jy)$. Equation (3.25) can be rewritten as

$$j\sqrt{\frac{-z^*}{-v^*}}\tan\left(-2\pi\sqrt{(-v^*)(-z^*)}\right) = j\sqrt{\frac{z}{v}}^*\tan\left(-2\pi\sqrt{vz}^*\right) = (-j)\sqrt{\frac{z}{v}}^*\left[\tan\left(2\pi\sqrt{vz}\right)\right]^* = 1. \tag{2.68}$$

Using the polar form for the quantities $-z^*$ and $-v^*$, we get for the product and the quotient of the square roots that

$$\sqrt{(-z^*)(-v^*)} = \sqrt{|z||v|}\, e^{j(\phi_z+\pi)/2} e^{j(\phi_v+\pi)/2} = -\sqrt{|z||v|}\, e^{j(\phi_z+\phi_v)/2} = \sqrt{zv}^* \tag{2.69}$$

and

$$\sqrt{\frac{-z^*}{-v^*}} = \sqrt{\frac{|z|}{|v|}}\, e^{j(\phi_z+\pi)/2} e^{-j(\phi_v+\pi)/2} = \sqrt{\frac{|z|}{|v|}}\, e^{-j(\phi_z-\phi_v)/2} = \sqrt{\frac{z}{v}}^*. \tag{2.70}$$

The propagation constant for a DNG material is

$$\begin{aligned}\alpha + j\beta &= \pm j2\pi\sqrt{vz}^* \\ &= \pm j2\pi\sqrt{|v||z|}\, e^{j\Phi} = \pm j2\pi\sqrt{|v||z|}\,(\cos\Phi + j\sin\Phi).\end{aligned} \tag{2.71}$$

In this case, we select the $(-)$ sign so that the real part is positive and the imaginary part negative:

$$\alpha + j\beta = 2\pi\sqrt{|v||z|}\,(-j\cos\Phi + \sin\Phi). \tag{2.72}$$

3. Relationship between DPS and DNG Materials

A comparison between Equations (3.26) and (3.31) shows that the DNG equation is the complex conjugate of the DPS equation. We note that when z and z^* are solutions to Equations (3.24) and (3.25), respectively, both Equations (3.26) and (3.31) are real; the imaginary parts of the left hand sides are zero. Therefore, we conclude that if z is a solution to the DPS equation for a given v, then $-z^*$ will be a solution for the DNG equation for $-v^*$. This results in the symmetry between the DPS and DNG cases observed in Figures 10 and 11.

F. SUMMARY

In this chapter, the main focus was on the matched wave impedance concept, in which the wave impedance at the front surface of the reflector backed material layer is made equal to the intrinsic impedance of free space to produce no reflection.

The material configuration and electromagnetic parameter values of a single homogeneous layer of dielectric/magnetic material to produce zero specular reflection has been determined for both DPS and DNG layers. Moreover, we recognize that that the regions of both materials are the same with the regions of Figures 10 and 11 for *A-B* space for lossless materials that were mentioned in the Chapter II.

The equations based on this concept were solved numerically using computer simulations in order to plot universal design curves for zero specular reflection.

In the following chapter, simulations of materials in the free space environment are used to extract the effective permittivity and permeability from scattering parameters obtained from data in turn obtained from simulations in MWS.

IV. EXTRACTING EFFECTIVE PARAMETERS

A. INTRODUCTION

In this chapter, measurements of materials in a free space environment are used to extract the effective permittivity and permeability from scattering parameters. In order to verify the accuracy of scattering parameters generated from simulation using MWS, MATLAB is used to calculate the reflection and transmission coefficients and compare those generated from simulation.

B. RETRIEVAL METHOD

The retrieval method used in the following sections is based on the approach by Xudong Chen *et al* in [27] where the S-parameters are defined in terms of the reflection and transmission coefficients as

$$S_{11} = R \tag{4.1}$$

$$S_{21} = Te^{jk_o d} \tag{4.2}$$

where κ_o denotes the wave number in free space and d is the thickness of the material. The S parameters are related to refractive index n and impedance Z by

$$S_{11} = \frac{R_{01}\left(1-e^{j2n\kappa_o d}\right)}{1-R_{01}^2 e^{j2n\kappa_o d}} \tag{4.3}$$

$$S_{21} = \frac{\left(1-R_{01}^2\right)e^{jn\kappa_o d}}{1-R_{01}^2 e^{j2n\kappa_o d}} \tag{4.4}$$

where $R_{01} = \left(Z-1\right)/\left(Z+1\right)$.

The impedance Z and the refractive index n are

$$Z = \pm \sqrt{\frac{(1+S_{11})^2 - S_{21}^2}{(1-S_{11})^2 - S_{21}^2}} \tag{4.5}$$

and

$$e^{jn\kappa_o d} = X \pm j\sqrt{1-X^2}, \tag{4.6}$$

respectively, where $X = \left[2S_{21}\left(1-S_{11}^2+S_{21}^2\right)\right]^{-1}$. Since the MTM under consideration is a passive medium, the signs in Equations (4.5) and (4.6) are determined by the requirement

$$\mathrm{Re}(Z) \geq 0 \tag{4.7}$$

and

$$\mathrm{Im}(n) \geq 0. \tag{4.8}$$

The value of refractive index n can be determined from Equation (4.6) as

$$n = \frac{1}{\kappa_o d}\left\{\left[\mathrm{Im}\left[\ln\left(e^{j\kappa_o d}\right)\right] + 2m\pi\right] - j\left[\mathrm{Re}\left[\ln\left(e^{j\kappa_o d}\right)\right]\right]\right\} \tag{4.9}$$

where m is an integer related to the branch index of the real part of n. The imaginary part of n is uniquely determined, but the real part is complicated by the branches of the logarithm function.

It is a common method to determine Z and n from Equations (4.5) and (4.6) with the requirement of Equations (4.7) and (4.8). However, this method may fail in practice when $\mathrm{Re}(Z)$ and $\mathrm{Im}(n)$ are close to zero. Sometimes the sign of $\mathrm{Re}(Z)$ and $\mathrm{Im}(n)$ change due to small perturbations in S_{11} and S_{21} that is produced in experimental measurements or numerical simulations. In order to determine the correct sign of Z, two cases are distinguished. The first case is for $\left|\mathrm{Re}(Z)\right| \leq \delta$, where δ is a positive number and for which $\mathrm{Re}(Z) \geq 0$. In the second case, the sign of Z is chosen so that the

corresponding n has a non-negative imaginary part $(\mathrm{Im}(n) \geq 0)$, or equivalently $\left|e^{jn\kappa_o d}\right| \leq 1$. The index of refraction is derived from Equations (4.3) and (4.4) to get

$$e^{jn\kappa_o d} = \frac{S_{21}}{1 - S_{11}\left(\frac{Z-1}{Z+1}\right)}. \tag{4.10}$$

The method to precisely determine the branch of $\mathrm{Re}(n)$ can be found in [27].

C. RETRIEVAL USING GENERATED S-PARAMETERS FROM MWS

In this section, simulations are performed using MWS by CST, which uses the finite integration technique (FIT) in either the time or frequency domain in order to determine reflection and transmission properties of any given model. Extracting the data of the reflection S_{11} and transmission S_{21} coefficients, a calculation of the constitutive parameters from the impedance Z and the index of refraction n is perfomed. The results of the calculation of the constitutive parameters were compared with published data.

1. Model 1

The model that we used in the first case is a cube with side length 2.5 mm. The material is given the constitutive parameters ε_r=5 and μ_r=3. The boundary conditions that are used are $H_t = 0$ and $E_t = 0$ as shown in Figure 13. These boundary conditions replicate an infinite slab with a plane wave normally incident at the ports as shown in Figure 14.

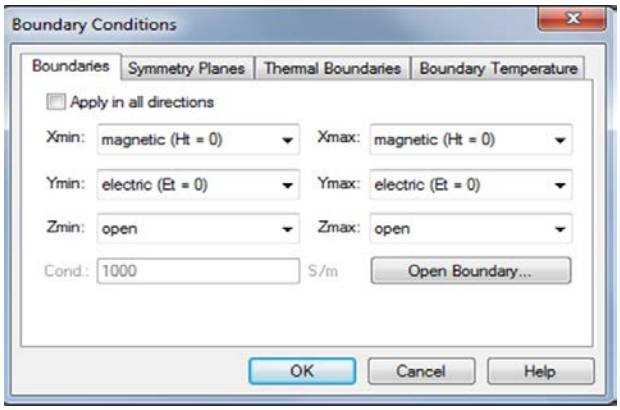

Figure 13. Boundary conditions for the cube (Model 1).

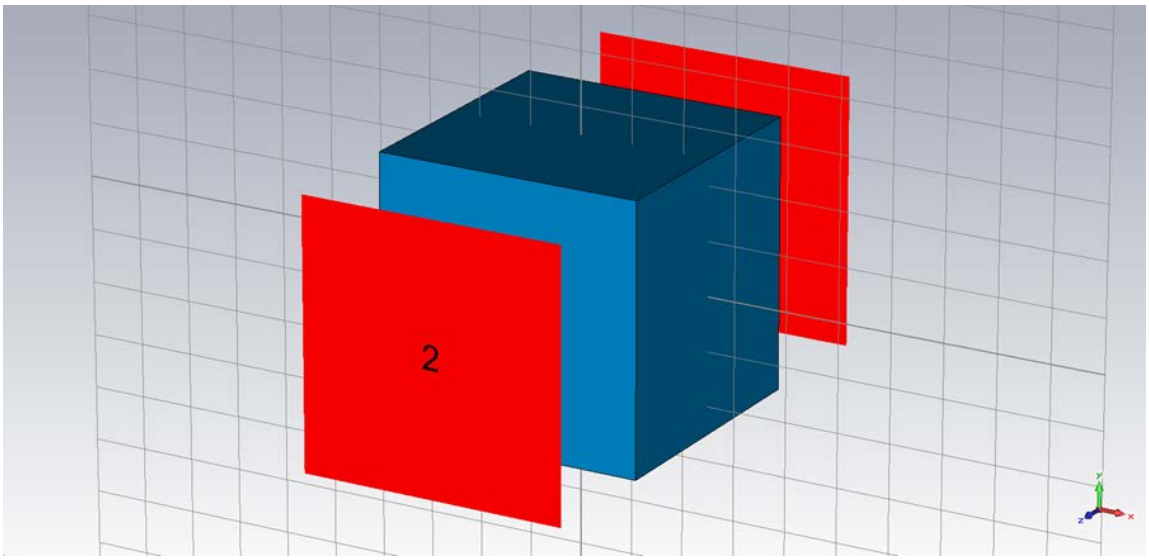

Figure 14. Cube with 2.5 mm side length and ε_r =5 and μ_r =3.

Running the simulation in MWS, we obtain the S-parameter magnitudes S_{11} and S_{21} in dB as shown in Figures 15 and 16, respectively.

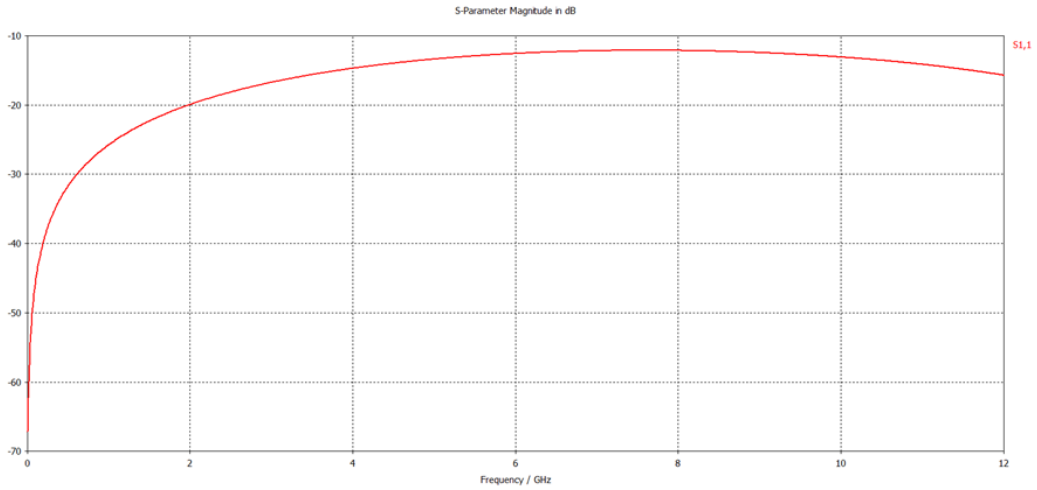

Figure 15. S_{11} magnitude in dB versus frequency for the Cube model.

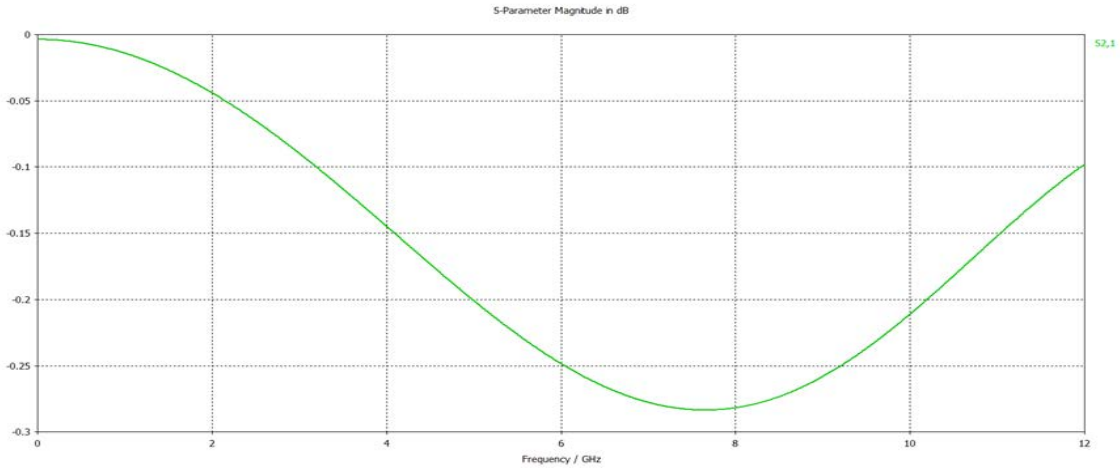

Figure 16. S_{21} magnitude in dB versus frequency for the Cube model.

For the same model and data, an extraction program [17] was used to retrieve the permeability and permittivity from the scattering parameters generated by MWS. The results of the extracted μ_r and ε_r using MATLAB are shown in Figures 17 and 20, respectively.

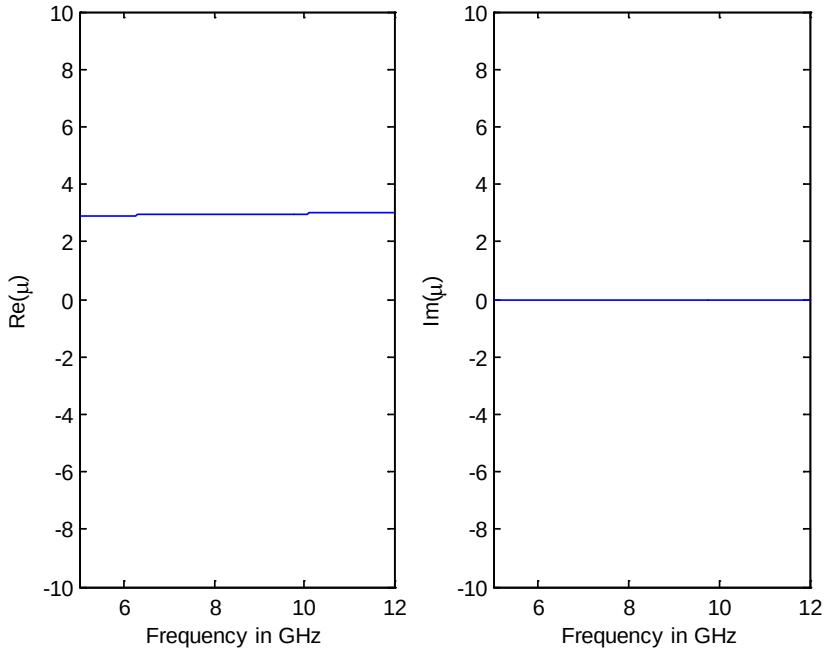

Figure 17. Extracted real and imaginary part of the permeability of the Cube model.

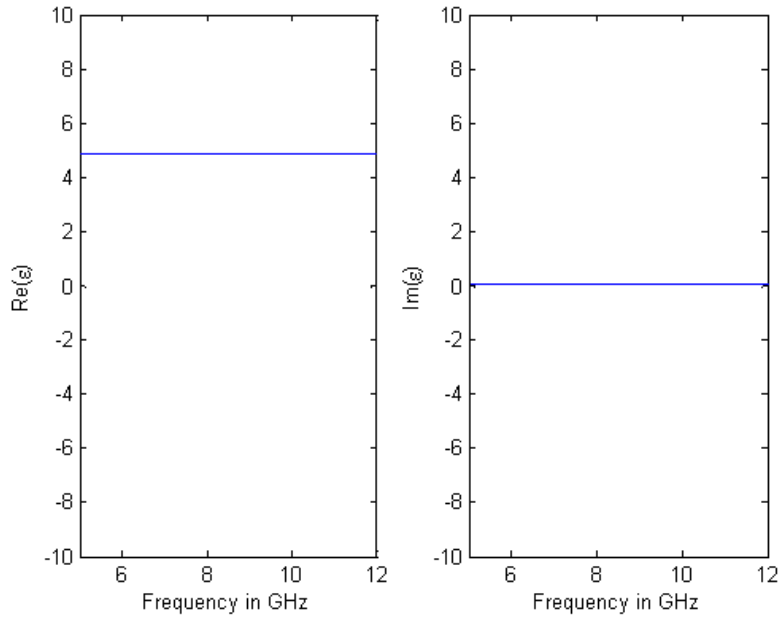

Figure 18. Extracted real and imaginary part of the permittivity of the Cube model.

The results of the extracted index of refraction and impedance for Model 1 are shown in Figures 19 and 20, respectively.

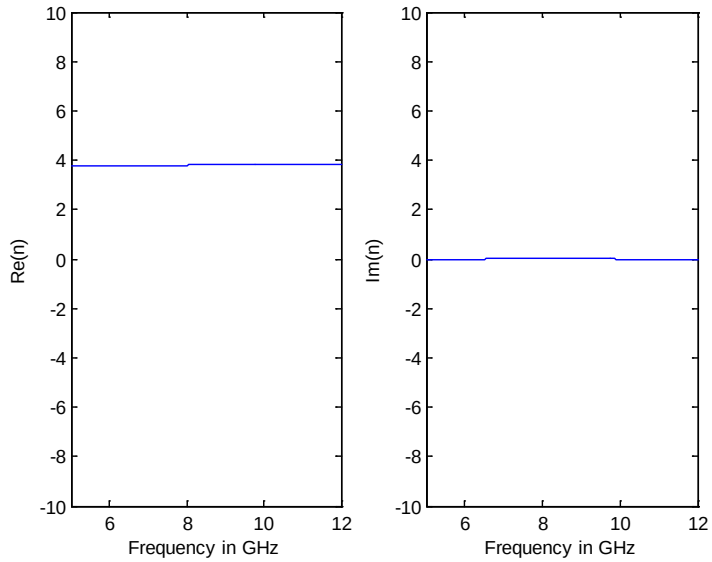

Figure 19. Extracted real and imaginary part of the index of refraction of the Cube model.

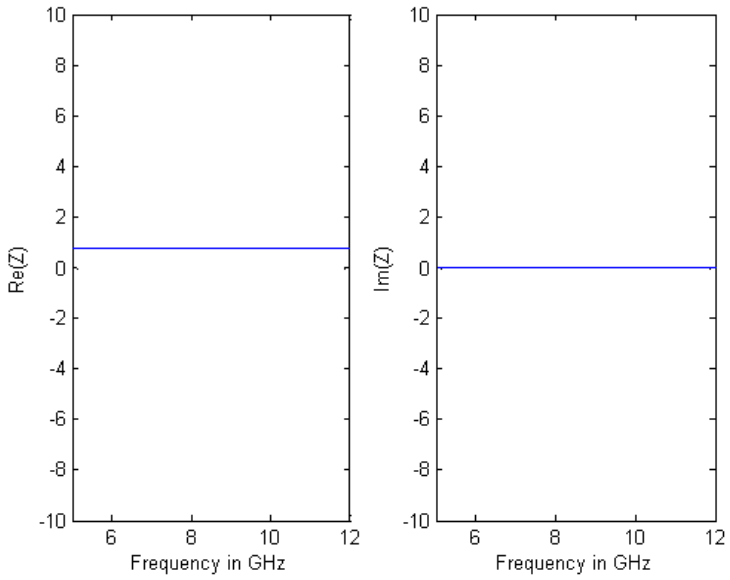

Figure 20. Extracted real and imaginary part of the impedance of the Cube model.

Note that the retrieval program extracts $\varepsilon = 5 \text{ and } \mu = 3$ from the simulation data. Thus, the retrieval program works correctly for RH materials whose constitutive parameters are both positive. In the following models, the process is extended to LH materials.

2. Model 2

This model is a "traditional" MTM, consisting of two split ring resonators (SRR) combined to form a coplanar ring (CPR) on a dielectric slab (see Figure 21). The dimensions of this model are the same as described in [28] and [29] and shown in Figure 21. More specifically, the inner ring radius r of the SRR is 1.5 mm, the ring width c is 0.8 mm, the radial gap width between the rings d is 0.2 mm and the dielectric thickness t is 0.216 mm. The dielectric slab is a square with length 5 mm and ε_r =3.2.

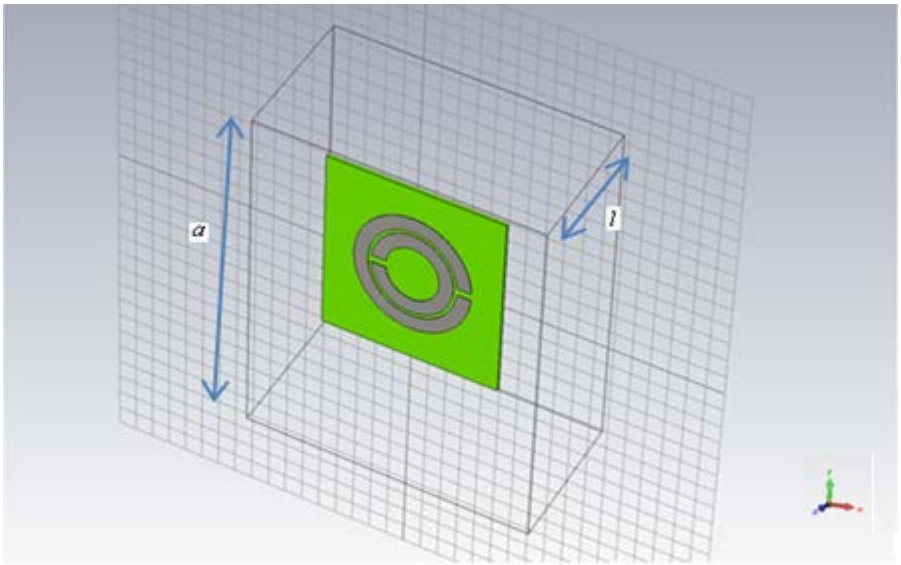

Figure 21. CPR with dimensions r =1.5 mm, d =0.2 mm, c =0.8 mm and t =0.216 mm.

The objective of this simulation is to calculate the effective permeability and permittivity from the extracted data of MWS. An analytical and theoretical approximation for the effective permeability of an SRR as a function of frequency is [29]

$$\mu_{eff}^{SRR} = 1 - \frac{\pi r^2}{a^2\left(1 - \frac{3d}{\varepsilon_o \mu_o \omega^2 \pi^2 r^3} + j\frac{2\sigma}{\mu_o \omega r}\right)} \tag{4.11}$$

where r and d are the same quantities as we described above, a is the lattice constant (separation distance between the centers of the rings), and σ is the resistance of the ring material. In our model a =8 mm and $\sigma = 0.0155\,\mathrm{S/m}$. A plot of $\mu_{eff}^{SRR}(f)$ as a function of the frequency in GHz is shown in Figure 22. In the derivation of Equation (4.11), it was assumed that the rings are close together in a matrix so that the magnetic field lines approximate those in a continuous cylinder [29].

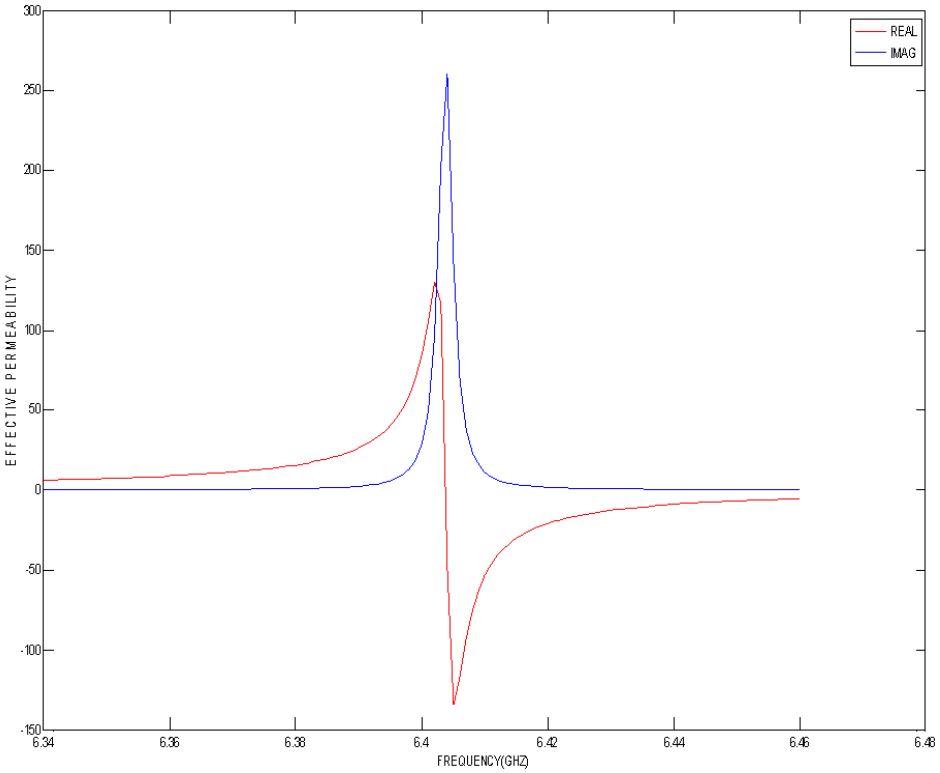

Figure 22. Effective permeability μ_{eff}^{SRR} for r =0.8 mm, a =8 mm, d =0.2 mm and $\sigma = 0.0155\,\mathrm{S/m}$.

The red line is the real part of the effective permeability and the blue line is the imaginary part, respectively. From Figure 22 we notice that the resonant frequency at which the effective magnetic permeability becomes negative and the left-handed behavior becomes evident is around 6.4 GHz for the SRR. The expression for the resonant frequency in GHz for the SRR is [28]

$$f_{res}^{SRR} = \frac{\sqrt{\dfrac{3d}{\mu_o \varepsilon_o \pi^2 r^3}}}{2\pi 10^9}(\mathrm{GHz}). \qquad (4.12)$$

Using this information for the model 2, we ran the simulation for three different cases. In each case, we used different boundary conditions in order to calculate the resonant frequency and to compare this frequency with the theoretical one.

a. Case I-Electric and Magnetic Boundaries

In first case, we set up open in the x- direction, electric $E_t = 0$ in the y-direction and magnetic H_t=0 in the z- direction. The plane waves propagate in the negative z direction. The boundary conditions that were used are shown in Figure 23.

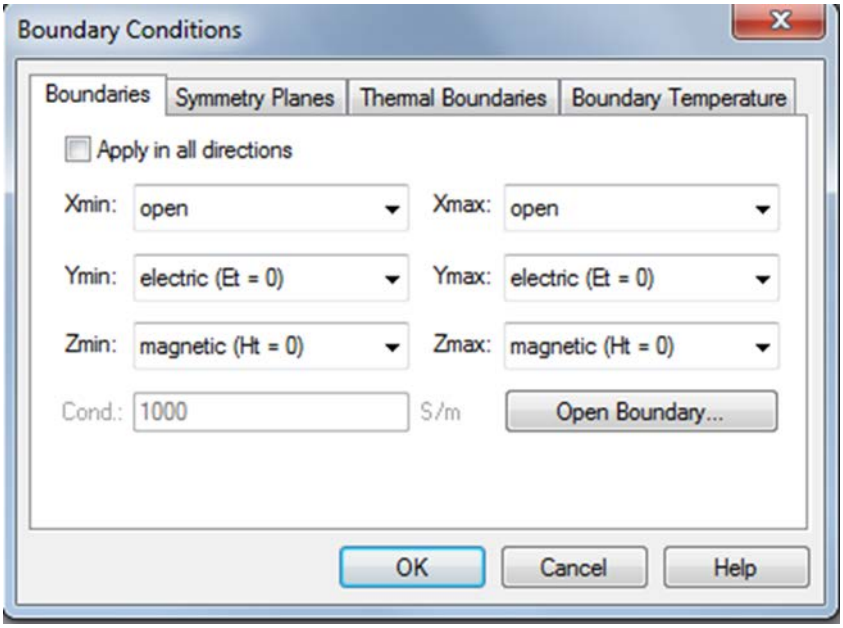

Figure 23. Boundary conditions for Model 2 Case I.

Running this simulation in MWS, we get the S-parameter magnitudes S_{11} and S_{21} in dB shown in Figures 24 and 25, respectively.

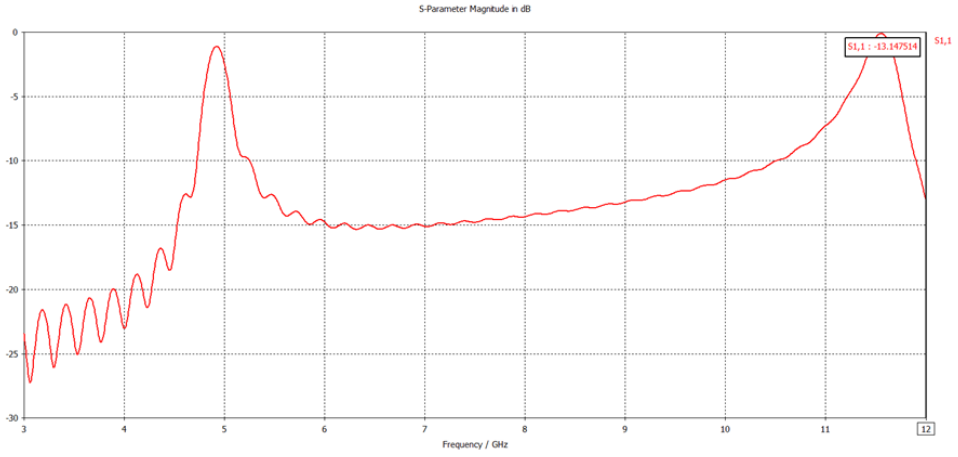

Figure 24. S_{11} magnitude in dB versus frequency for Model 2 Case I.

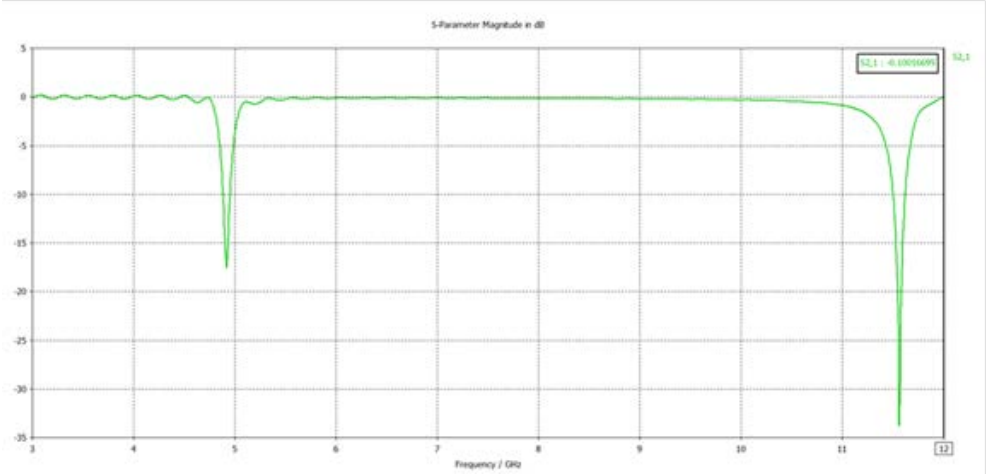

Figure 25. S_{21} magnitude in dB versus frequency for Model 2 Case I.

The simulation results are very sensitive to the setting of “mesh cells” in MWS. Different mesh cells can generate slightly different resonant frequencies. One way to avoid this uncertainly is to use the function “adaptive mesh refinement” in MWS. This function is able to calculate the S-parameters with different mesh cells until the difference between the S-parameters is less than the specified value. This method can ensure that the mesh size is small enough to make the result stable.

The extracted permittivity, permeability, index of refraction, and impedance are shown in Figures 26 through 29.

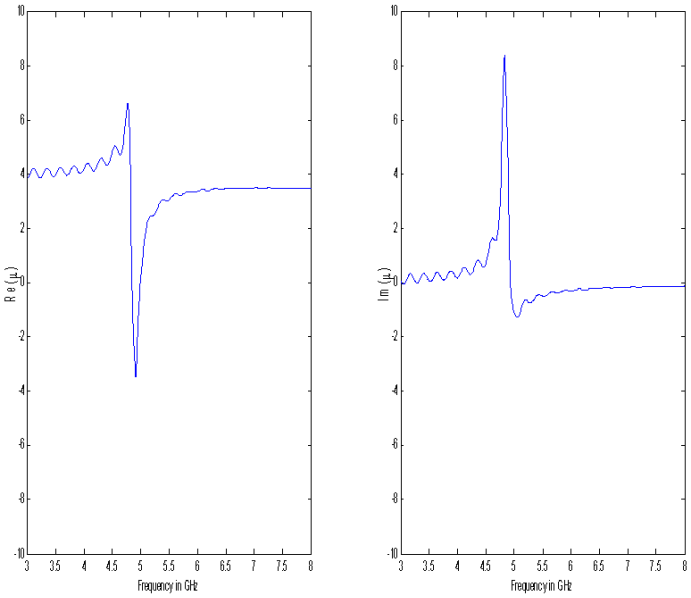

Figure 26. Extracted permeability of Model 2 Case I.

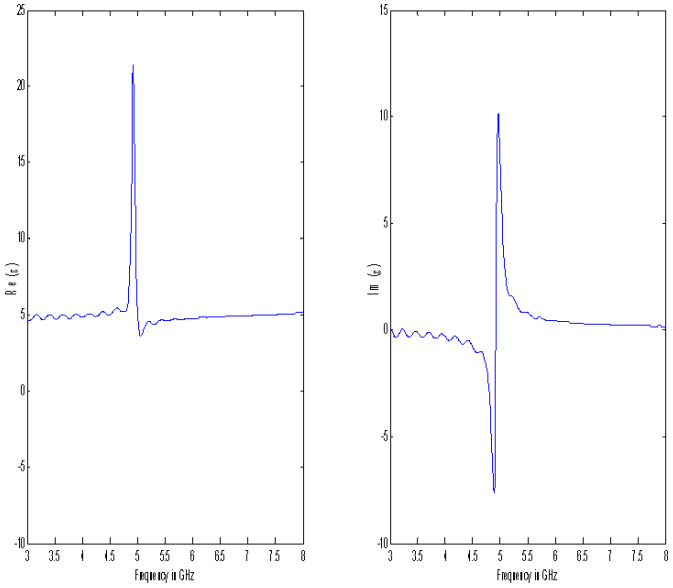

Figure 27. Extracted permittivity of Model 2 Case I.

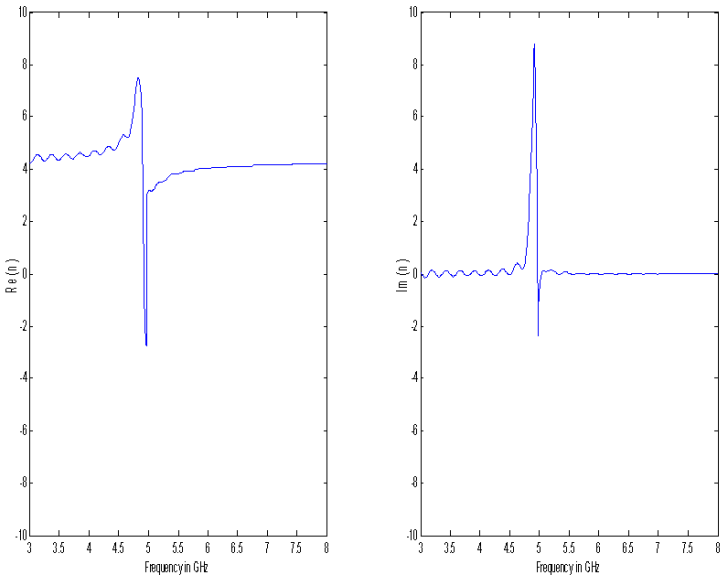

Figure 28. Extracted index of refraction of Model 2 Case I.

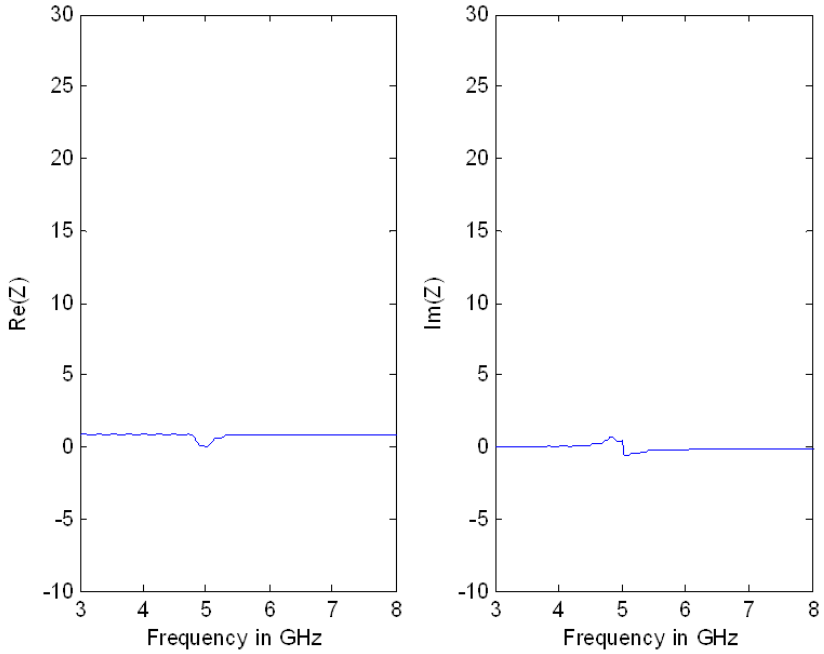

Figure 29. Extracted impedance of Model 2 Case I.

The extracted constitutive parameters, index of refraction, and impedance of the material are very close to the published data [28]. Moreover, the simulated parameters are very close to the published data (the resonant frequency is close to 4.86 GHz as in [28] and [29]). Because the authors do not refer to any details about the meshing parameters that they used, the final results are not identical to the published data, but they appear to be very close (by inspection).

b. Case II-Open Boundaries

In the second case, we set up open (add space) in the x-direction, open (add space) in the y-direction and open in the z-direction, as shown in Figure 30. The model with these boundary conditions is shown in Figure 31. The calculated S-parameters S_{11} and S_{21} from MWS in dB are given in Figures 32 and 33, respectively.

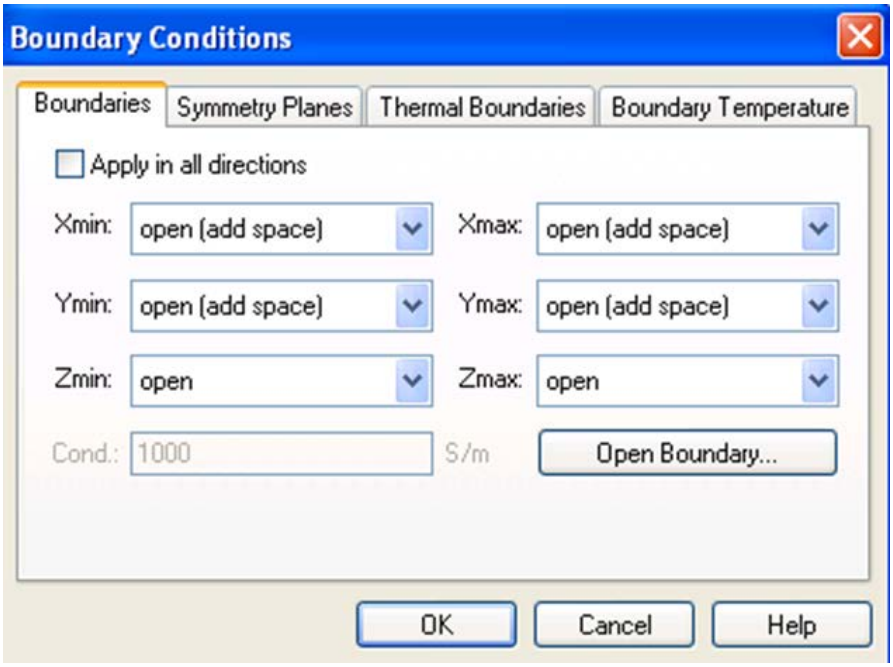

Figure 30. Boundary Conditions for Model 2 in Case II.

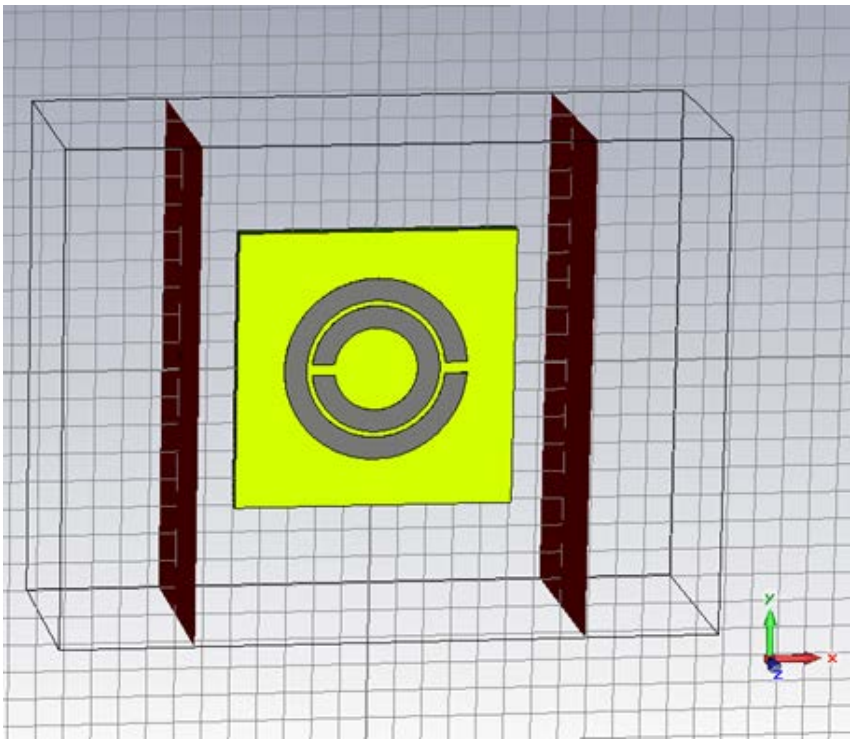

Figure 31. Model 2 case II.

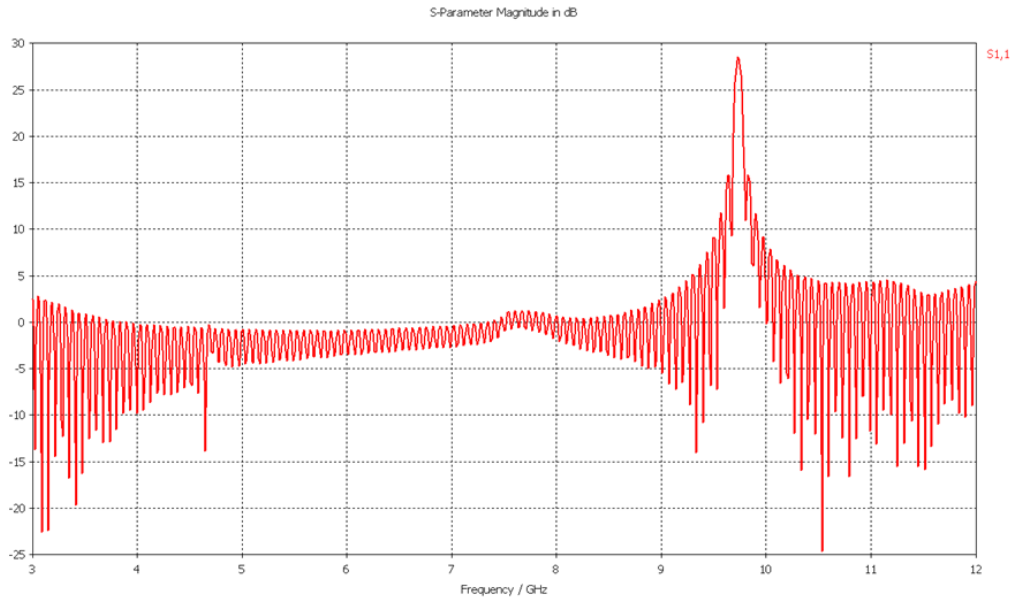

Figure 32. S_{11} magnitude in dB versus frequency for Model 2 Case II.

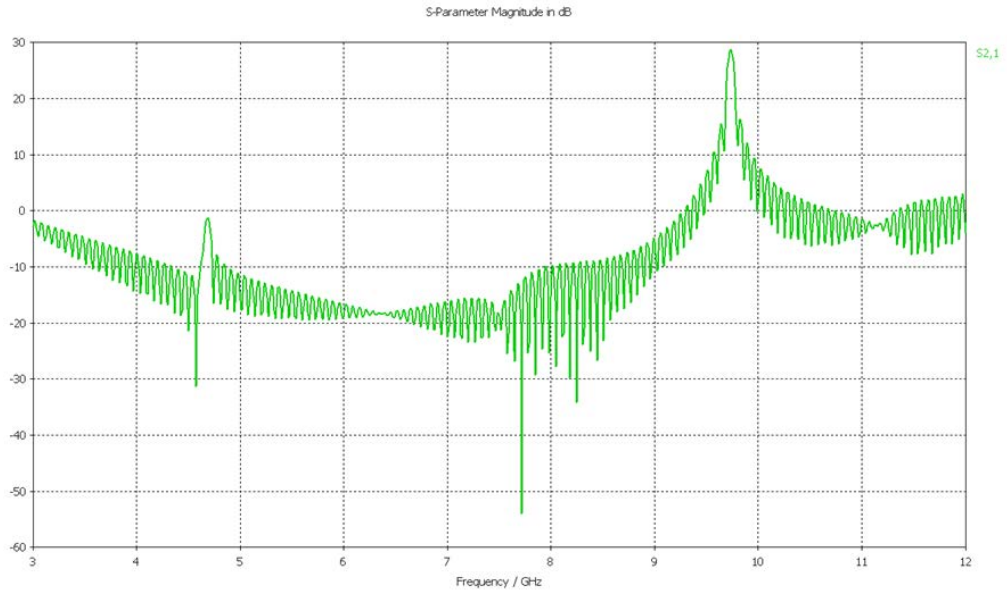

Figure 33. S_{21} magnitude versus frequency for Model 2 Case II.

The extracted permittivity, permeability, index of refraction, and impedance were not calculated because the scattering parameters are for only an isolated ring in free space. The scattering in this case is entirely different from what it would be for the CPR in a matrix. As shown in Figure 37, the resonant frequency for the calculated S_{21} parameter from MWS is very close to 4.86 GHz, which is the same as calculated in Case I.

c. Case III-Unit Cell

For the last case for this model, we set up unit cells in the x-direction, unit cells in the y-direction and open in the z-direction. Note that the model has been rotated compared to the previous case. This is because the unit cells can only be excited from Floquet ports $Z_{\max}$ and $Z_{\min}$ at the top and bottom of the model. Each unit cell is square with a cell dimension of $a = l$ =8 mm. The model and the boundary conditions that are used are shown in Figures 34 and 35, respectively.

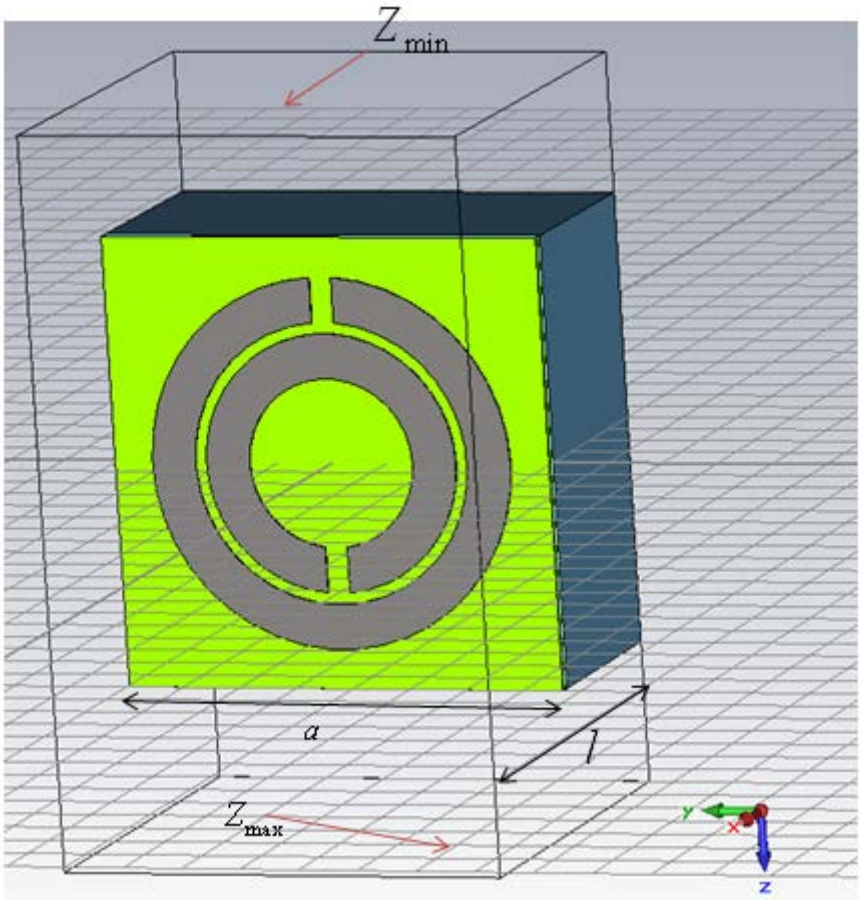

Figure 34. Model 2 for Case III built in MWS with SRR and square unit cell with side with length 8 mm.

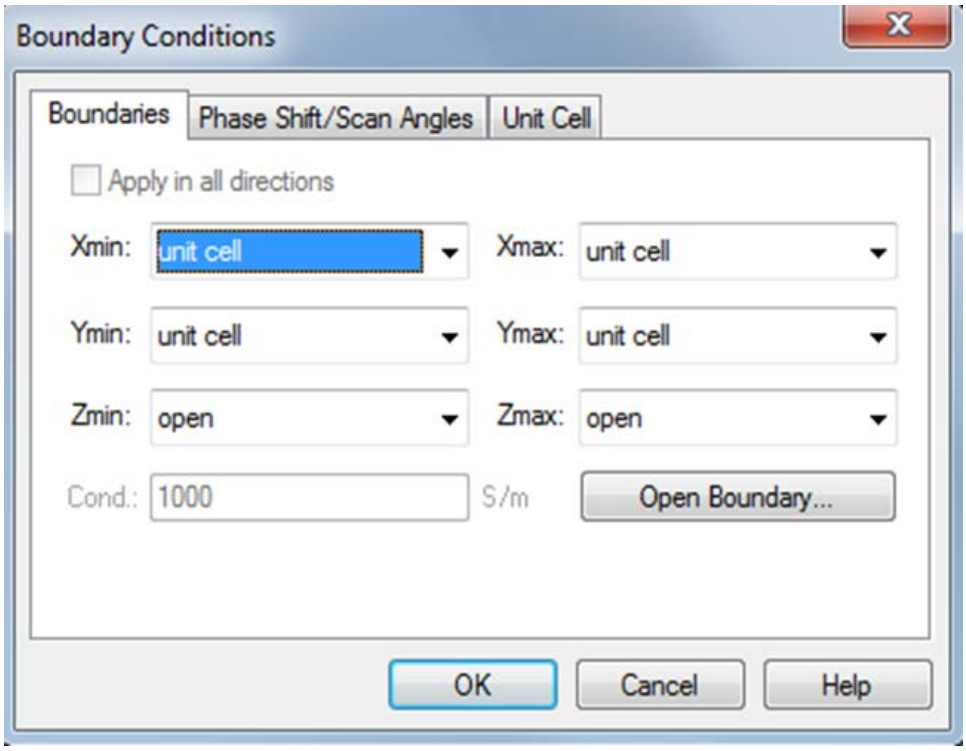

Figure 35. Boundaries conditions for Model 2 Case III

The calculated S-parameters S_{11} and S_{21} from the MWS in dB are given in Figures 36 and 37, respectively.

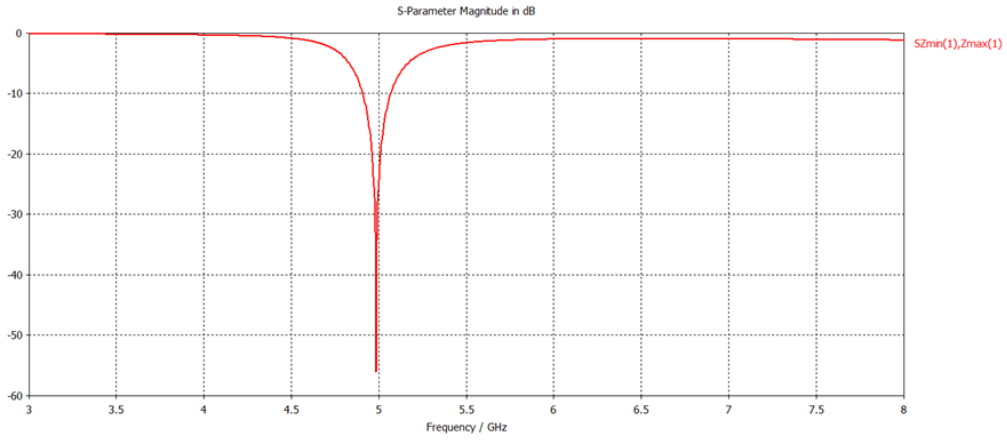

Figure 36. S_{11} magnitude in dB for Model 2 Case III.

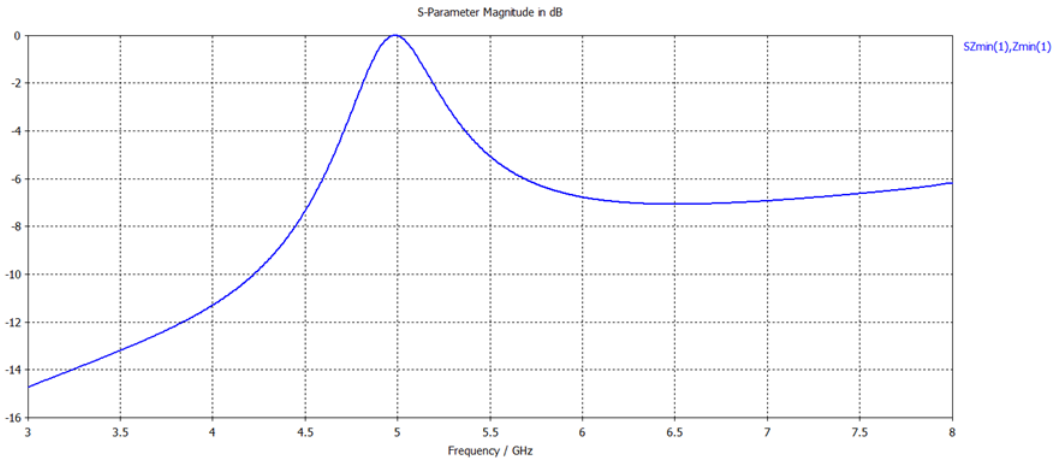

Figure 37. S_{21} magnitude in dB versus frequency for Model 2 Case III.

The extracted permittivity, permeability, index of refraction, and impedance are shown in Figures 38 through 41.

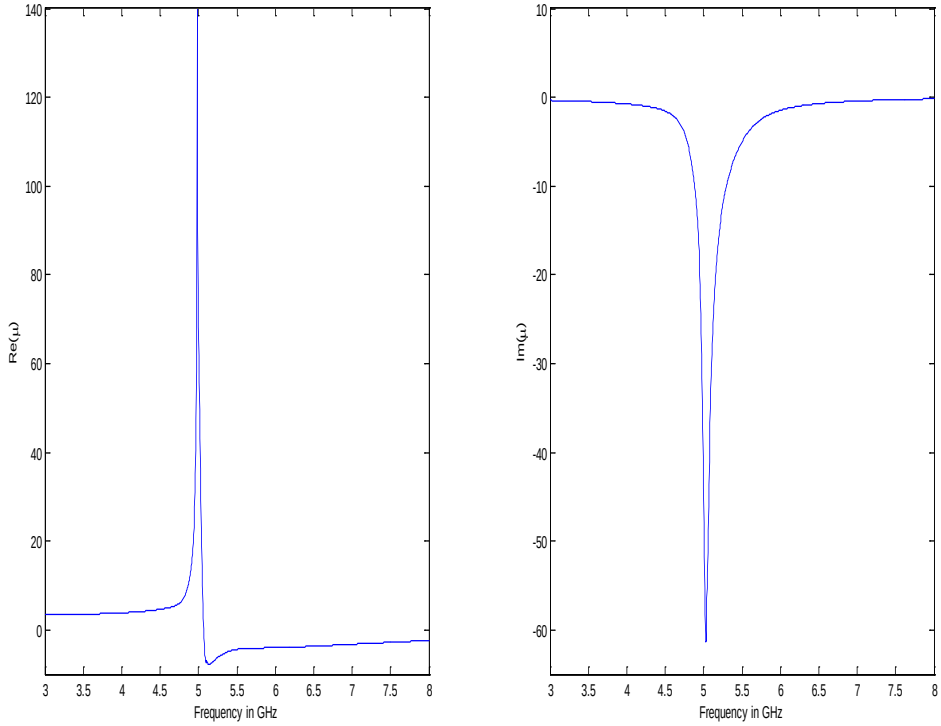

Figure 38. Extracted permeability of Model 2 Case III.

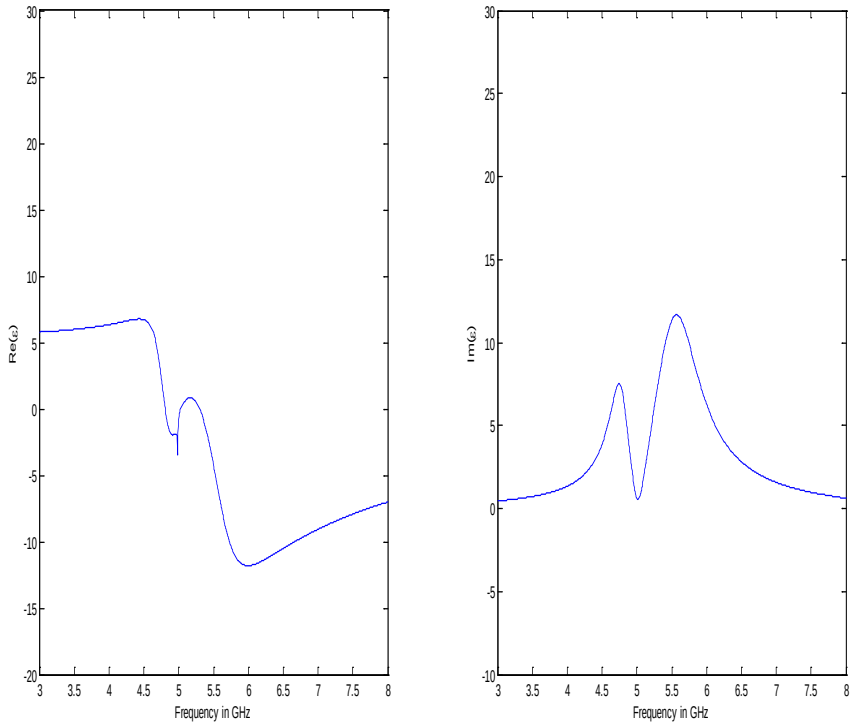

Figure 39. Extracted permeability of Model 2 Case III.

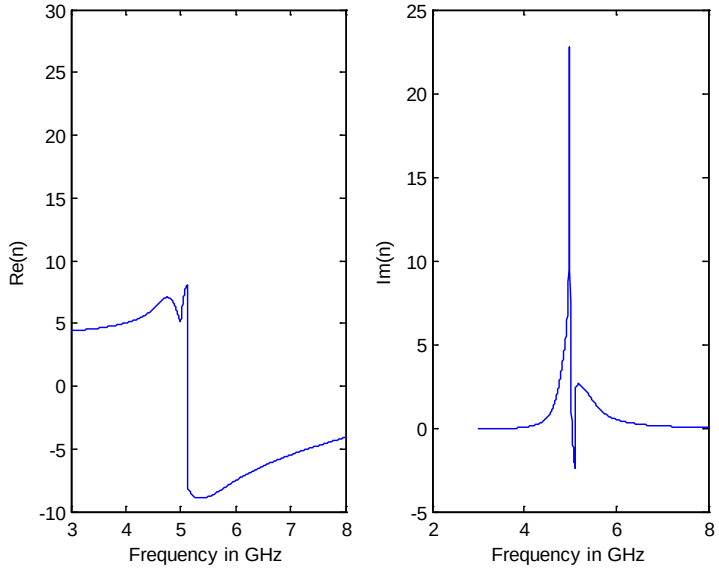

Figure 40. Extracted index of refraction of Model 2 Case III.

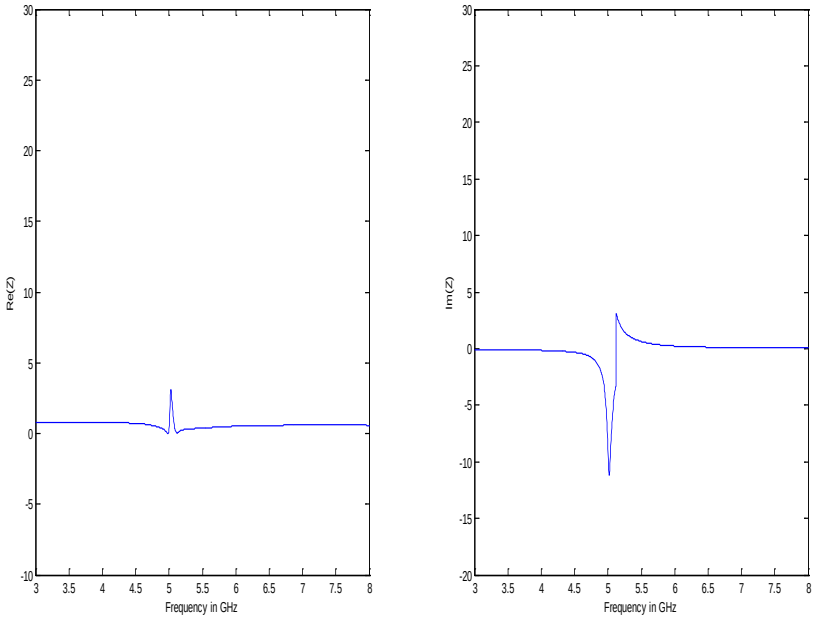

Figure 41. Extracted impedance of Model 2 Case III.

For Case III of this model, we notice that the resonant frequency is close to the calculated resonant frequency of MWS and the published data and has a value 4.916 GHz. That means that the simulation works correctly, but a problem appeared in the extraction of the constitutive parameters. Notice from Figure 38 that the curve for the real part is the same as the theoretical value of the imaginary part. Many test cases were executed for this model by changing the range of frequency, the adaptive parameters, the number of Floquet modes (tests executed for mode 1 through mode 25) and the distance to the reference plane and essentially the same results were obtained.

3. Model 3

The third model that was used to test the effectiveness of the extraction program is based on the same CPR structure proposed in [30]. The dielectric slab has the same dimensions as Model 2, but the dimensions of SRR are different in this construction. More specifically, the inner ring radius r of the SRR is 2 mm, the ring width c is 1 mm, the radial gap width between the rings d is 0.1 mm and the dielectric thickness t is 0.216 mm. Model 3 is shown in Figure 42.

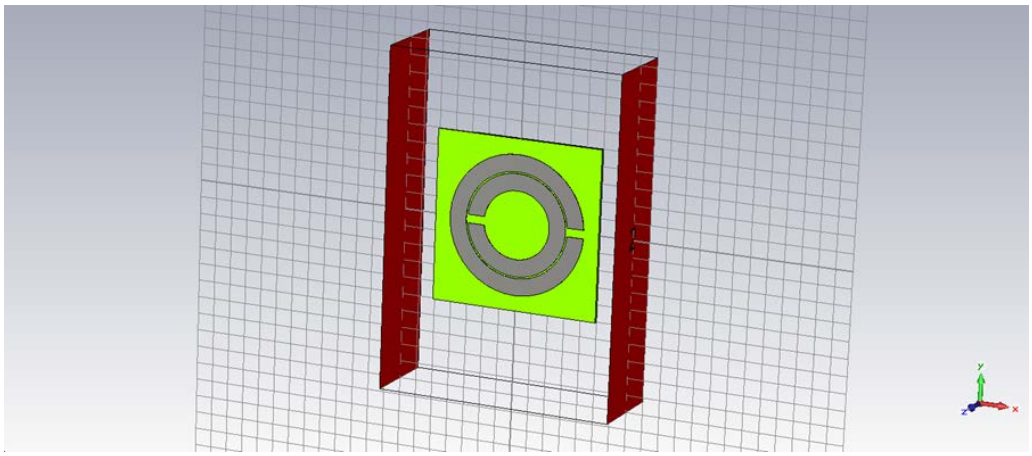

Figure 42. Model 3- SRR with r =2 mm, d =0.1mm, c =1 mm and t =0.216 mm.

Using the theoretical background of [30], we arrive that the effective magnetic permeability for SRR is given by Equation (4.11).The resonant frequency at which μ_{eff}^{SRR} becomes negative is given by Equation (4.12).

For Model 3, we calculate the resonant radian frequency to be $\omega_o = 7.1\times10^{21}$ rad/sec and, thus, the resonant frequency is 13.5 GHz. From Equation (4.12) we notice that the resonant frequency scales uniformly with size; if we double the size of all elements in a given structure, the resonant frequency halves. This observation is shown in Figures 43 and 44, in which we plot the μ_{eff}^{SRR} for a SRR with two different values for the resistance of the ring material (σ_1=200 for copper rings and σ_2 for resistive rings). The result is that the resonant frequency appears at 13.5 GHz in both cases. In both figures the red lines represent the real part of μ_{eff}^{SRR} and the blue lines the imaginary part, respectively.

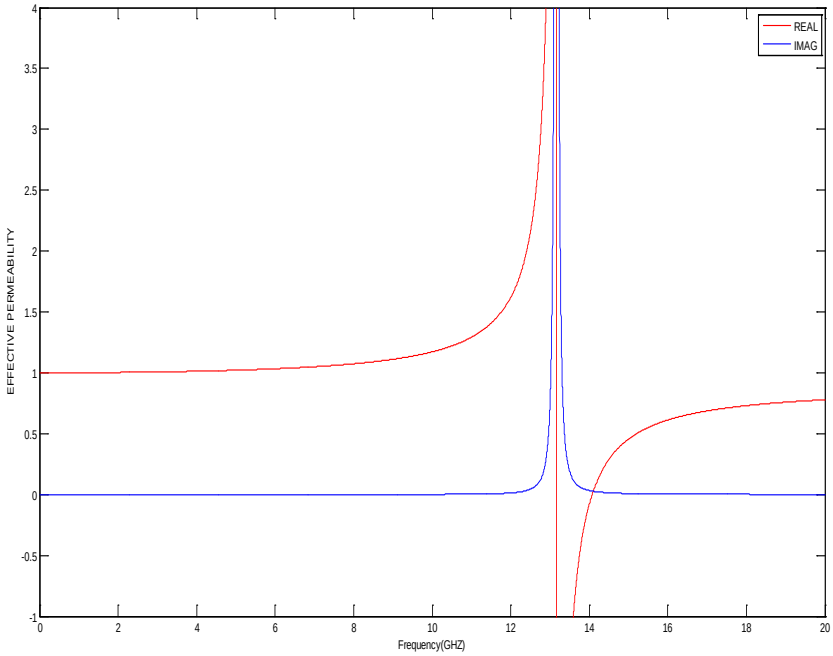

Figure 43. Plot of μ_{reff}^{SRR} for Model 3 using cooper rings σ_1=200 S/m.

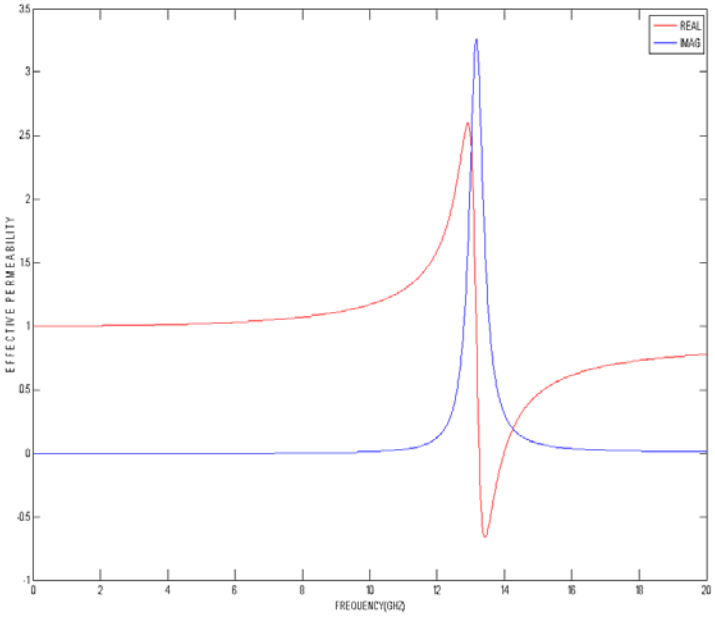

Figure 44. Plot of μ_{reff}^{SRR} for Model 3 using resistive rings σ_1 =2000 S/m.

Using these dimensions for the Model 3, we ran the simulation for two different cases, using different boundary conditions in order to calculate the resonant frequency and to check this frequency with the theoretical result.

a. Case I-Electric and Magnetic Boundaries

In this case, we set up open in the x-direction, $E_t = 0$ in the y-direction and H_t=0 in the z-direction, as shown in Figure 45.

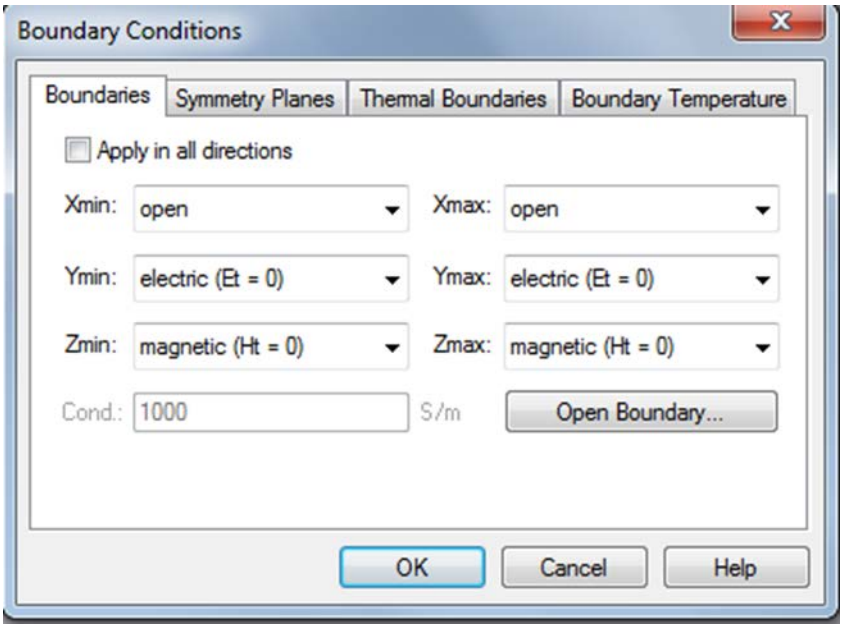

Figure 45. Boundary conditions for Model 3 Case I.

Running this simulation, we obtained the results in Figures 46 and 47 for the S-parameters S_{11} and S_{21} in dB, respectively.

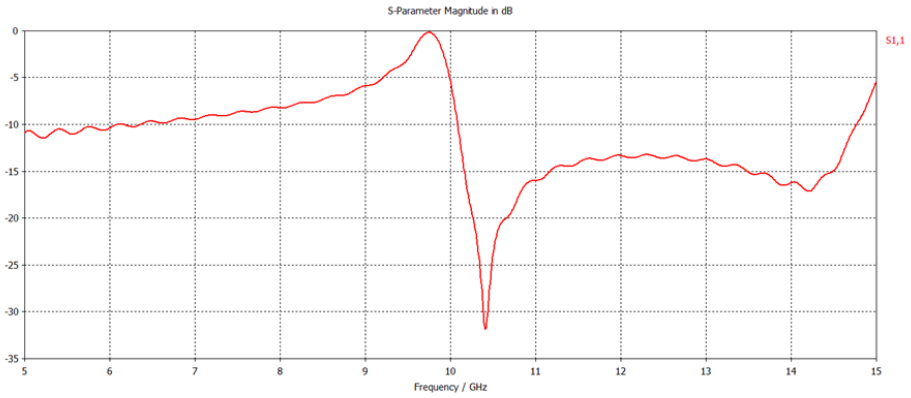

Figure 46. S_{11} magnitude in dB versus frequency for Model 3 Case I.

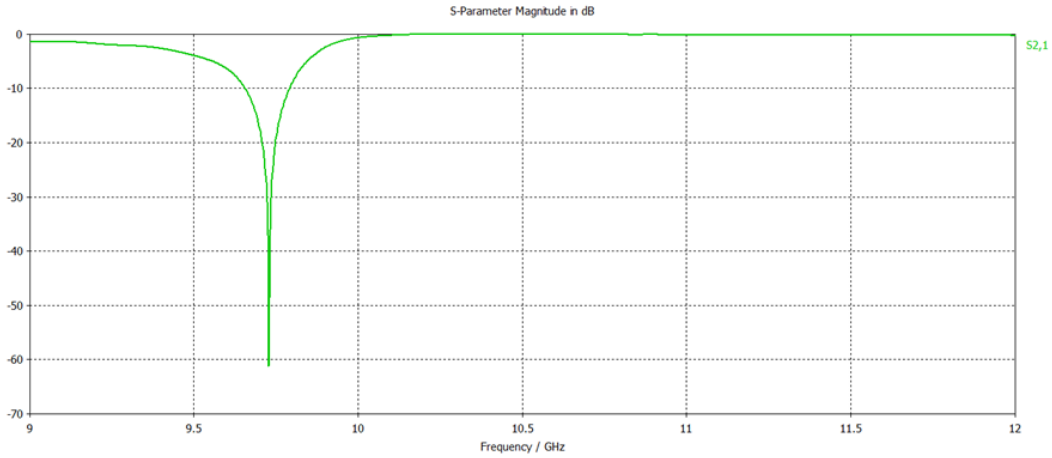

Figure 47. S_{21} magnitude in dB versus frequency for Model 3 Case I.

The extracted permittivity, permeability, index of refraction, and impedance are shown in Figures 48 through 51.

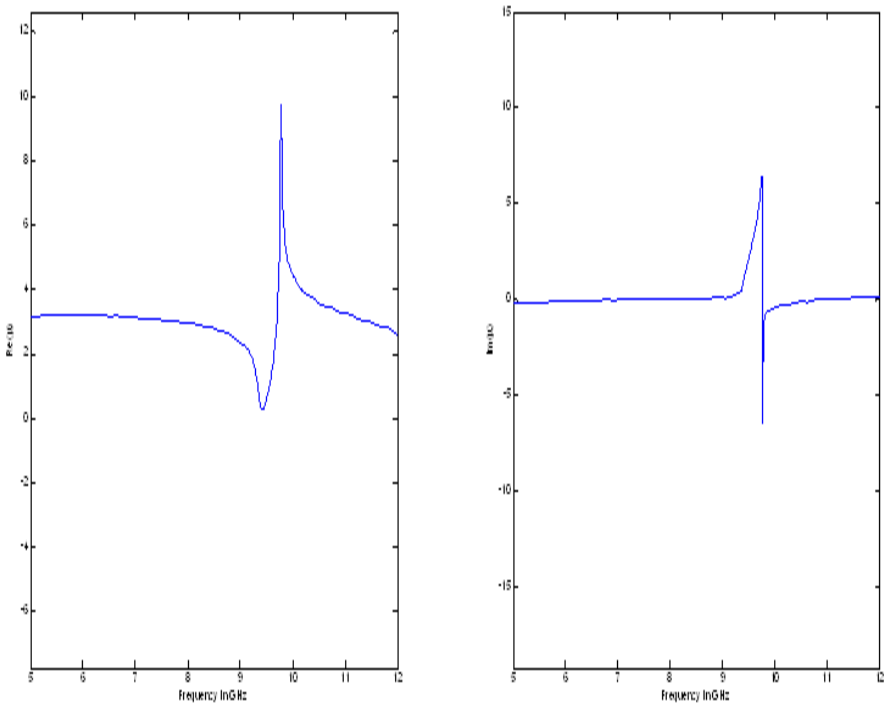

Figure 48. Extracted permeability of Model 3 Case I.

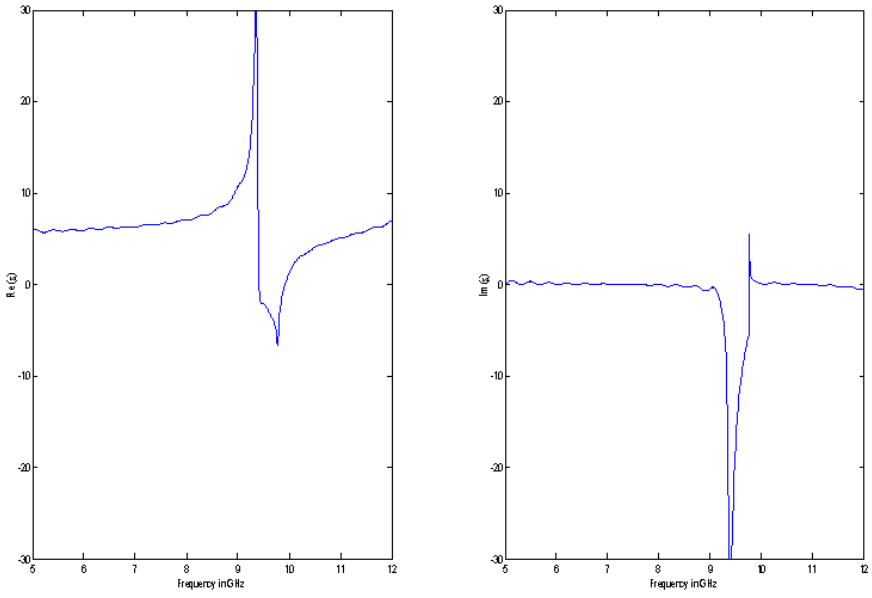

Figure 49. Extracted permittivity of Model 3 Case I.

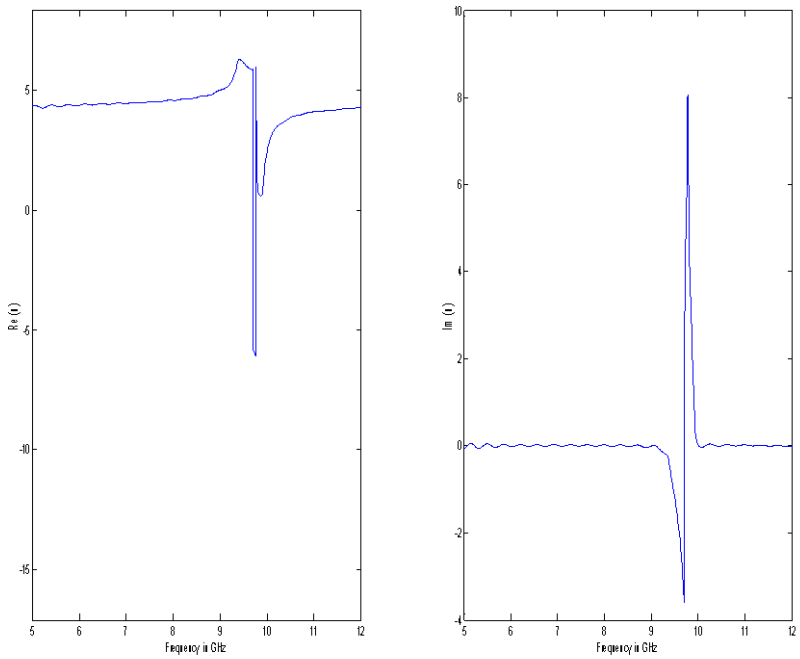

Figure 50. Extracted index of refraction of Model 3 Case I.

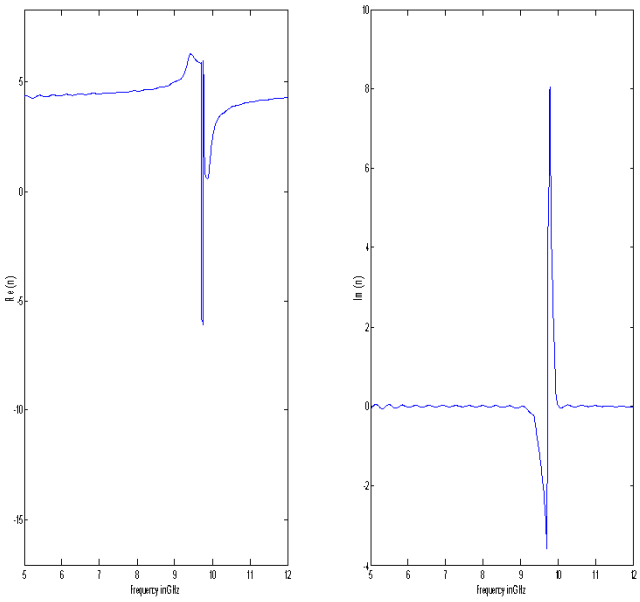

Figure 51. Extracted impedance of Model 3 Case I.

From Figure 46, we see that the calculated resonant frequency for the S_{21} parameter is close to 9.8 GHz, and from the extracted constitutive parameters we notice that the resonant frequency is close to the same value. In the published data, the authors do not refer any calculated values for the S-parameters from MWS or for the extracted constitutive parameters. They refer only to the theoretical resonant frequency value, which is 13.5 GHz. Because we calculated the same resonant frequency both from S_{21} and the extracted permittivity and permeability, the final results are not identical to the published data, although they are correct.

b. Case II-Unit Cell

In this second case for this model, we set up a unit cell in the x-direction, a unit cell in the y-direction and open in the z-direction. Each unit cell has dimensions of a=10 mm and l=2 mm and is placed in each side of the SRR in the negative z-direction. The model and the boundary conditions that are used are shown in Figures 52 and 53, respectively.

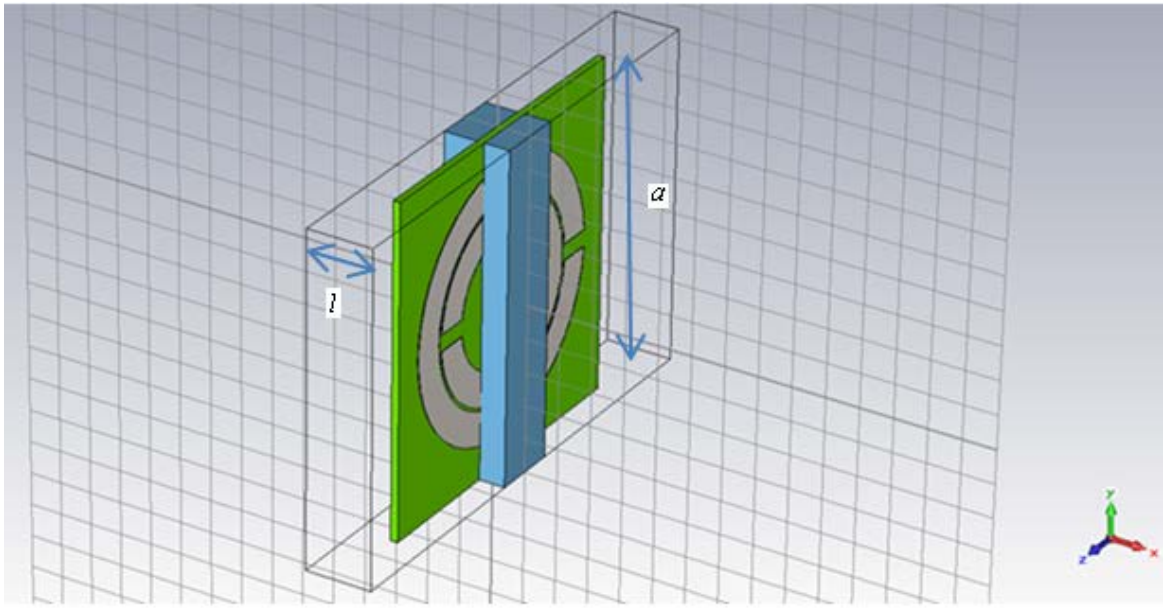

Figure 52. Model 3 Case II.

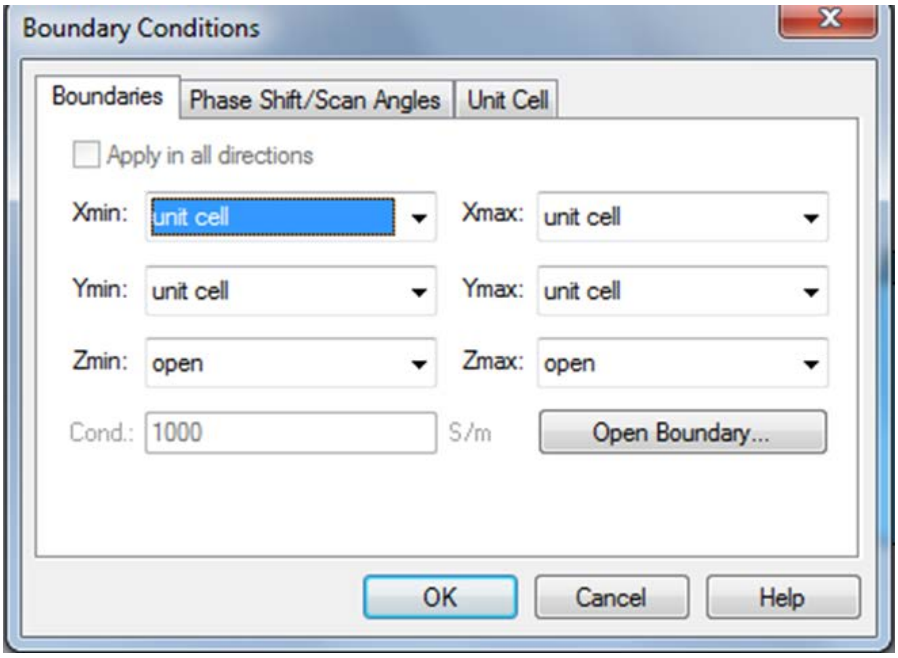

Figure 53. Boundary conditions for Model 3 Case II.

Running this simulation, we obtained the results in Figures 54 and 55 for the S-parameters S_{11} and S_{21} in dB, respectively.

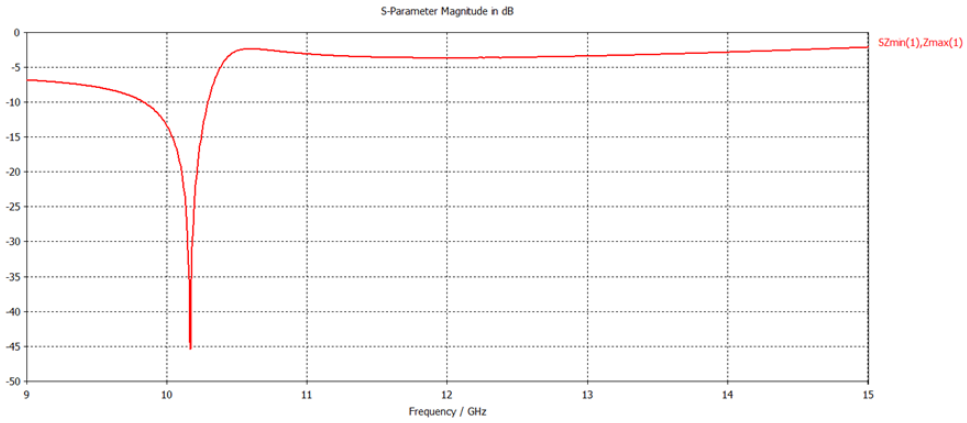

Figure 54. S_{11} magnitude in dB versus frequency for Model 3 Case II.

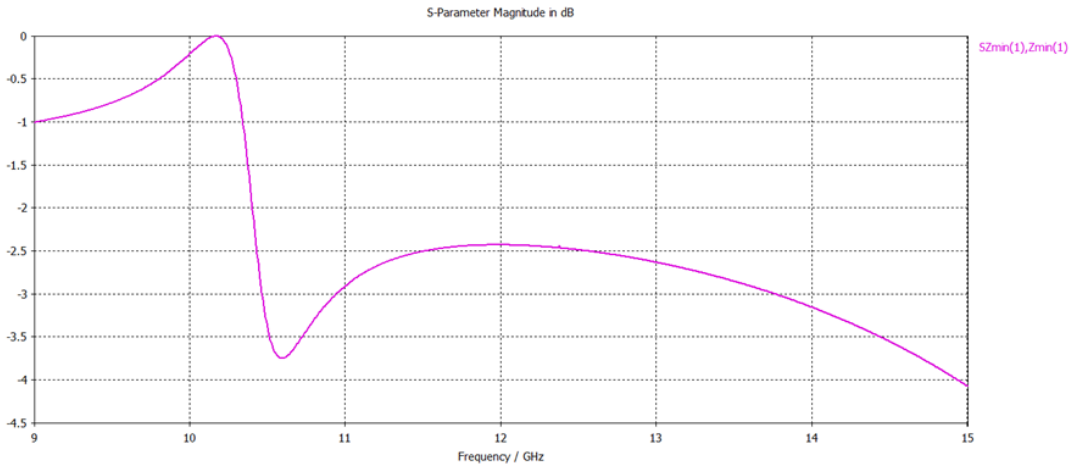

Figure 55. S_{21} magnitude in dB versus frequency for Model 3 Case II.

The extracted permittivity, permeability, index of refraction, and impedance are shown in Figures 56 through 59.

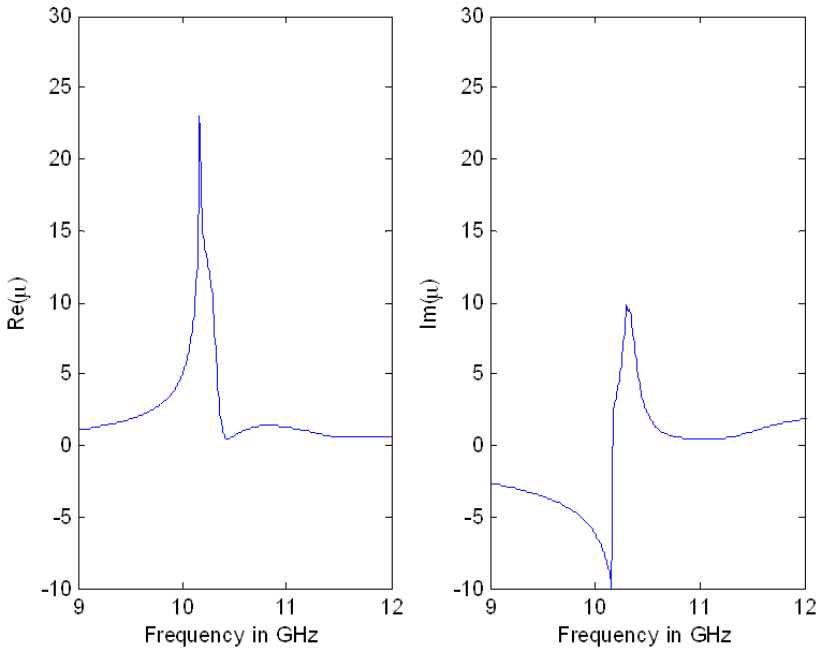

Figure 56. Extracted permeability of Model 3 Case II.

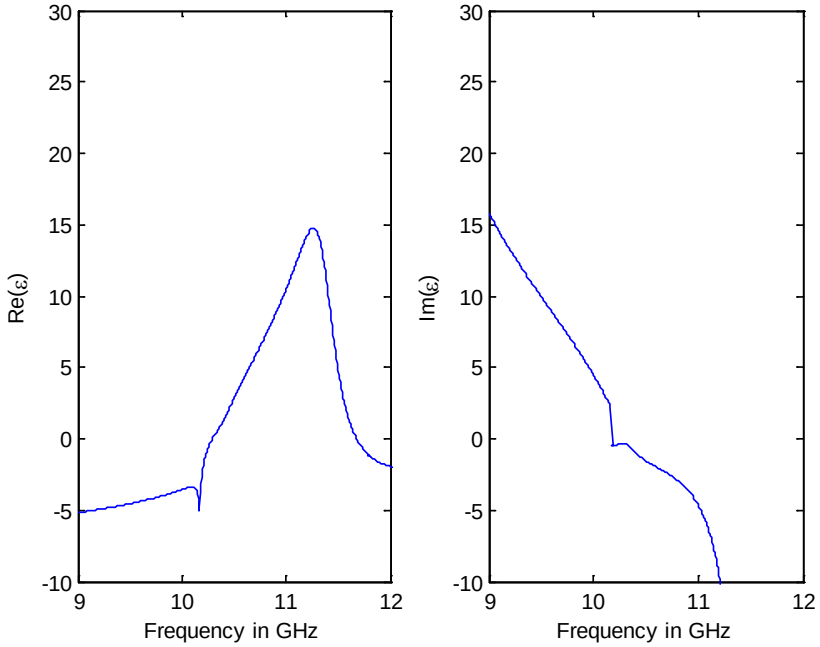

Figure 57. Extracted permittivity of Model 3 Case II.

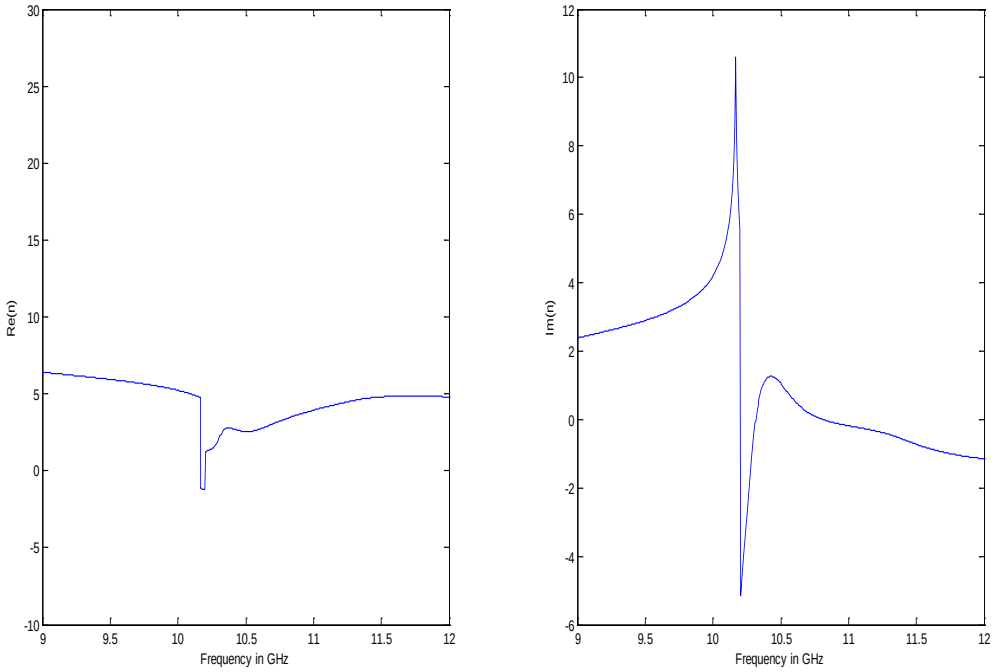

Figure 58. Extracted index of refraction of Model 3 Case II.

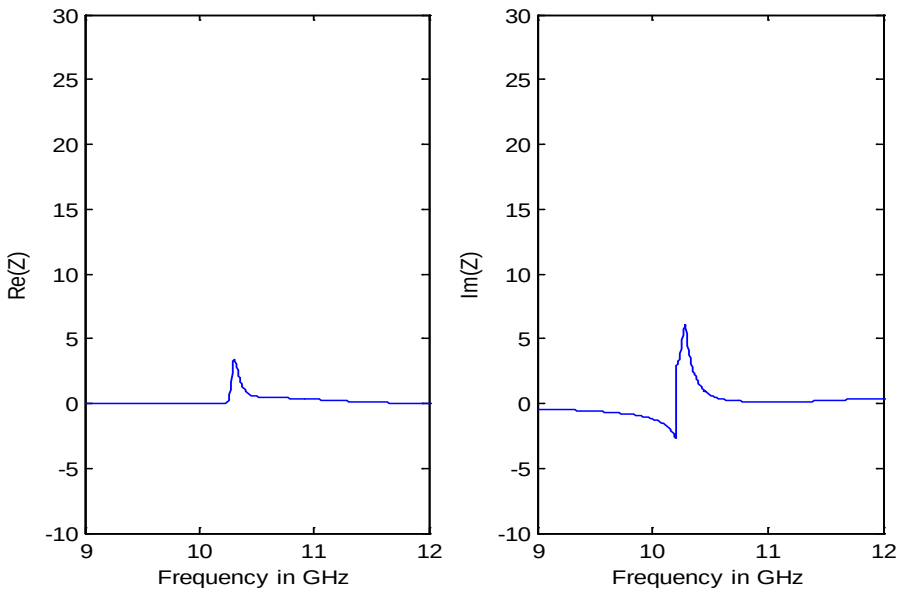

Figure 59. Extracted impedance of Model 3 Case II.

In this model, we saw the same problems as those that appeared in Model 2 Case III. Again, we obtained incorrect curves for the permeability, but the calculated resonant frequency is about 10 GHz and coincides with the resonant frequency of the extracted constitutive parameters.

D. SUMMARY

In this chapter, three models were used to extract the permeability and permittivity from the S-parameters. The formula used was based on the free space environment, and many different boundary conditions were used in order to check the calculated S-parameters. The calculated S-parameters were used in a MATLAB program in order to extract the constitutive parameters. The resonant frequency is very sensitive to the number of mesh cells and the dimensions of the model; therefore, it is helpful to have the simulation, the measurements and the published data for comparison purposes. The above models have shown that the extraction program can work for normal and MTMs.

Problems were encountered with the unit cell boundary conditions. The extracted data were not as expected. This should be investigated in future research. There may be some additional phase weights that have to be applied to the Floquet results before the extraction can be perfomed.

THIS PAGE INTENTIONALLY LEFT BLANK

V. CONCLUSION

A. SUMMARY AND CONCLUSIONS

The basic concept and the unusual characteristics of MTMs were discussed in this thesis. Based on this introduction, the unusual properties of DNG were discussed, and an analysis of each property was presented. A classification of lossy materials depending on the signs of ε_r' and μ_r' was defined in terms of A and B parameters. We classified the different types of MTMs according to the triads of RH and LH.

In the first part of this research, an analysis of zero specular absorbers was presented, and all the equations related to specular absorbers were analyzed based on transmission line theory. Numerical solutions of the equations were used to generate the universal design curves for zero specular reflection layers. A solution of the transcendental equation resulting from our analysis was given for a PEC backing. Moreover, a solution for the transcendental equation for both DPS and DNG layers was programmed in MATLAB 7.4 in order to characterize the behavior of metamaterials. The results showed that both a DPS and a DNG layer follow similar curves of the universal design chart, and that the DNG solution is the complex conjugate of the DPS solution for the same a and b values. Thus, symmetry between DPS and DNG solutions was obtained.

In the second part of this thesis, a retrieval program was used to extract the permittivity and permeability of MTM models that were simulated in MWS. The equations for the S-parameters in a free space environment were described and programmed in MATLAB. Different types of materials, including "normal" material and MTMs, were simulated in MWS, and the results were exported to the MATLAB program in order to calculate the real and the imaginary parts of the permittivity, permeability, index of refraction and impedance. The results were compared with published data. The resonant frequency of the results and its relationship to the dimensions of the models were found to agree.

It was shown that the key parameters for a successful retrieval was the correct selection of the number of mesh cells used at the simulation staring point, the dimensions of the model, the boundary condition setting in MWS and the background materials.

The results using simulated scattering parameters were in good agreement with available published data when electric and magnetic boundaries were used in MWS. Agreement was not good when using unit cell boundaries and Floquet modes. This discrepancy is likely due to the form of the Floquet mode fields and how they are converted to scattering parameter data for use in the Matlab script. This should investigated further in subsequent research.

B. FUTURE WORK

In this thesis, DPS and DNG materials were used to examine the solutions of transcendental equation based on the transmission line theory. SNG materials were not included. Due to the sign ambiguity of the product of the square root $\pm\sqrt{\mu\varepsilon}$, the right decision of the sign is crucial when using SNG materials. Future research could address SNG materials in order to generate the universal design chart and to determine whether there is any symmetry in the solutions of the transcendental equation between DPS-DNG and SNG.

Furthermore, future work should include SNG materials to examine the retrieval programs. Based on the scattering parameters, it should be possible to extract parameters for SNG materials.

Finally, future work should include an investigation of the CST simulations with unit cell boundaries to determine the source of error in the extracted μ and ε.

APPENDIX

A. MATLAB CODE FOR UNIVERSAL CHART

The MATLAB code used to generated the universal curves for DPS and DNG layers in Chapter III is provided in this section. The code is written in MATLAB 7. This code plots a sample universal curve for fixed values of α and β, the solution of transcendental equation for both DPS and DNG layers and the solutions in $A-B$ space.

```
% solve transcendental equation for matched RAM layer over PEC backing
% generate a curve on the universal chart
% USING EXPLICIT SIGNS IN z for DNG block
clear
clc
% set tan delta curve
tandel=2;
% 'a' positive values
A=logspace(-3,1,500);
% 'b' positive values for search
B=A*tandel;
N=length(A);
Tol=1e-20;  % fsolve tolerance
SOL='DPS';  % solve for DPS with PEC backing
% start of search range for each curve
if SOL=='DNG', x_est=0; y_est=0; end
if SOL=='DPS', x_est=0; y_est=0; end
msg=['Computing...'];
hwait=waitbar(0,msg);
%%%%%%%%%%%%%%%%%%%%%%%%%%%%%%%%%%%%%%%%%%%%%%%%%%%%%%%%%%%%%%%%%%%%%%%%
%%%%%%%%%%%%%%%%%%%%%%%%%%%%%%%%%%%%%%%%%%%%%%%%%%%%%%%%%%%%%%%%%%%%%%%%
%%%%%%%%%%%%%%%%%%%%%%%%%%%%%%%%%%%%%%%%%%%%%%%%%%%%%%%%%%%%%%%%%%%%%%%%
% solution for DPS case
if SOL=='DPS'
    for n=1:N
        waitbar(n/N,hwait);
% a and b are POSITIVE in the transcendental equation
        a=A(n);
        b=B(n);
        [z fval]=fsolve(@(X) transcend_DPS_PEC_pos(X,a,b), [x_est;
y_est],...
            optimset('TolFun',Tol,'Display','off'));
% save values for check
        x(n)=z(1);
        y(n)=-z(2);
        W(n)=x(n)+j*y(n);   % this is x-j*y
        zz(n)=z(1)+j*z(2);
        Z(n)=sqrt(zz(n)/(a-j*b));
        G=sqrt((a-j*b)*zz(n));
```

```
        Gam(n)=G*j;
% Lee and Park A and B parameters
        AA(n)=x(n)*a-y(n)*b;
        BB(n)=y(n)*a+b*x(n);
    end
close(hwait);
% single panel plot
    figure(1)
    clf
    subplot(221)
    loglog(x,y,'xk')
    xlabel('x=t/\lambda*\mu_r_e_a_l')
    ylabel('y=t/\lambda*\mu_i_m_a_g')
    title([num2str(SOL),', tan\delta=',num2str(tandel)])
    subplot(222)
    plot(real(zz),imag(zz),'ko')
    title([num2str(SOL),' solution, z=z_1+jz_2, z_1=x, z_2=-y'])
    xlabel('real part, z_1 or x')
    ylabel('imaginary part, z_2 or -y')
    subplot(223)
    plot(real(Gam),imag(Gam),'ko')
    title([num2str(SOL),' propagation constant \gamma=\alpha+j\beta'])
    xlabel('\alpha, Np/m')
    ylabel('\beta, rad/m')
    subplot(224)
    plot(BB,AA,'k+')
    title('A-B classification space')
    ylabel('(t/\lambda) A')
    xlabel('(t/\lambda) B')
    Lmax=floor(max([max(abs(AA)),max(abs(BB))]))+1;
end     % end of DPS block
%%%%%%%%%%%%%%%%%%%%%%%%%%%%%%%%%%%%%%%%%%%%%%%%%%%%%%%%%%%%%%%%%%%%%%%%%%%%%%%
%%%%%%%%%%%%%%%%%%%%%%%%%%%%%%%%%%%%%%%%%%%%%%%%%%%%%%%%%%%%%%%%%%%%%%%%%%%%%%%
%%%%%%%%%%%%%%%%%%%%%%%%%%%%%%%%%%%%%%%%%%%%%%%%%%%%%%%%%%%%%%%%%%%%%%%%%%%%%%%
% solution for DNG case
if SOL=='DNG'
    for n=1:N
        waitbar(n/N,hwait);
% a and b are the negative of these values in the transcendental
equation
        a=A(n);
        b=B(n);
        [z fval]=fsolve(@(X) transcend_DNG_PEC_neg(X,a,b), [x_est;
y_est],...
            optimset('TolFun',Tol,'Display','off'));
% save values for check
        x(n)=z(1);    % let x be negative
        y(n)=z(2);
        W(n)=-x(n)-j*y(n);   % both x and y are positive
        zz(n)=-z(1)-j*z(2);   % solution to equation
        Z(n)=sqrt(-zz(n)/(-a-j*b));
        if real(Z(n))<0, Z(n)=-Z(n); end
        G=sqrt(zz(n)*(-a-j*b));
% choose solution with positive alpha
        Gam(n)=G*j;
```

```
        if real(G*j)<0, G=-G; Gam(n)=-Gam(n); end    % alpha > 0 always
% Lee and Park A and B parameters
        AA(n)=x(n)*a-y(n)*b;  % for new solution x<0 for DNG
        BB(n)=-y(n)*a-b*x(n);
    end
close(hwait);
% single panel plot
    figure(2)
    clf
    subplot(221)
    loglog(x,y,'xk')
    xlabel('x=t/\lambda*\mu_r_e_a_l')
    ylabel('y=t/\lambda*\mu_i_m_a_g')
    title([num2str(SOL),', tan\delta=',num2str(tandel)])
    subplot(222)
    plot(real(zz),imag(zz),'ko')
    title([num2str(SOL),' solution, z=z_1+jz_2, z_1=-x, z_2=-jy'])
    xlabel('real part, z_1 or -x')
    ylabel('imaginary part, z_2 or -y')
    subplot(223)
    plot(real(Gam),imag(Gam),'ko')
    title([num2str(SOL),' propagation constant \gamma=\alpha+j\beta'])
    xlabel('\alpha, Np/m')
    ylabel('\beta, rad/m')
    subplot(224)
    plot(BB,AA,'k+')
    title('A-B classification space')
    ylabel('(t/\lambda) A')
    xlabel('(t/\lambda) B')
    Lmax=floor(max([max(abs(AA)),max(abs(BB))]))+1;
end     % end of DNG block
% saving final data for checking the solution manually
% column vectors of a, b, z1, z2, alpha, beta
K=[A.' B.' zz.' Gam.'];
```

B. MATLAB CODE FOR DPS PEC

The MATLAB code used to solve the transcendental function for DPS_PEC materials is provided below:

```
function F=transcend_DPS_PEC_pos(X,a,b)
% a and b are POSITIVE (DPS)
% create complex value from real and imaginary parts
z=X(1,:)+j*X(2,:);
% choose sign of impedance with positive resistance
Z=sqrt(z/(a-j*b));
if real(Z)<0, Z=-Z; end
% choose solution with positive alpha
G=sqrt((a-j*b)*z);
f=Z*tanh(j*2*pi*G)-1;       % using tanh (no dif with tan)
% separate real and imaginary parts
F=[real(f); imag(f)];
```

C. MATLAB CODE FOR DNG PEC

The MATLAB code used to solve the transcendental function for DNG_PEC materials is provided below:

```
function F=transcend_DNG_PEC_neg(X,a,b)
% a and b are POSITIVE
% create complex value from real and imaginary parts
z=-X(1,:)-j*X(2,:);
% choose sign of impedance with positive resistance
Z=sqrt(z/(-a-j*b));
if real(Z)<0, Z=-Z; end
% choose solution with positive alpha
G=sqrt(z*(-a-j*b));        % explicit Gam not needed
if real(G*j)<0, G=-G; end  % insures the correct sign (-)
f=Z*tanh(j*2*pi*G)-1;
% separate real and imaginary parts
F=[real(f); imag(f)];
```

LIST OF REFERENCES

[1] V. G. Veselago, " The electrodynamic properties of a mixture of electric and magnetic charges," *Journal of Experimental and Theoretical Physics,* vol. 25, p. 680, 1967.

[2] Ben A. Munk, *Metamaterials: Critique and Alternatives*, 2008.

[3] V. G. Veselago, "The electrodynamics of substance with simultaneously negative values of and ," *Sov. Phys. Usp*., vol. 10, no. 4, pp. 509–524, Jan. 1968.

[4] J. B. Pendry, A. J. Holden, W. J. Stewart & I. Young, "Extremely low frequency plasmons in metallic mesostructures,'' *Phys. Rev. Lett*., 76, 4773, (1996).

[5] N. Engheta, "Is Foster's reactance theorem satisfied in double-negative and single-negative media?" *Microwave Opt. Technol. Lett*., vol. 39, no. 1, pp. 11–14, Oct. 2003.

[6] D. R. Smith, "The reality of negative refraction," *Physics World*, May 2003.

[7] K. Yee "Numerical solution of initial boundary value problems involving Maxwell's equations in isotropic media," *IEEE Transactions on Antennas and Propagation*, vol. 14, no. 3, pp. 302–307, 1966.

[8] D. R. Smith, "Composite medium with simultaneously negative permeability and permittivity," *Phys. Rev. Lett,*. vol. 84, pp. 4184–4187, 2000.

[9] R. A. Shelby, D. R. Smith and S. Schultz, "Experimental verification of a negative-index of refraction," *Science,* vol. 292, pp. 77–79, 2001.

[10] D. H. Lee and W. S. Park, "A New Material Classification Of Lossy Metamaterials," *IEEE Trans. Microwave and Optical Technology Letters*, vol. 53, no. 2, p. 445, 2011.

[11] J. B. Pendry, A. J. Holden, D. J. Robbins, and W. J. Stewart, "Magnetism from conductors and enhanced nonlinear phenomena," *IEEE Trans. Microwave Theory Tech.*, vol. 47, pp. 2075–2084, 1999.

[12] J. B. Pendry, "Negative Refraction Makes a Perfect Lens," *Phys. Rev. Lett*., vol. 85, p. 3966, 2000.

[13] D. R. Smith, W. J. Padilla, D. C. Vier, S. C. Nemat-Nasser, and S. Schultz, "Composite medium with simultaneously negative permeability and permittivity," *Phys. Rev. Lett.*, vol. 84, no. 18, pp. 4184–4187, 2000.

[14] R. A. Shelby, D. R. Smith & S. Schultz, “Experimental Verification of a Negative Index of Refraction,’’ *Science*, vol. 292, p. 77, 2001.

[15] J. Zhou, T. Koschny, L. Zhang, G. Tuttle, C. M. Soukoulis, “Experimental demonstration of negative index of refraction,” *Applied Physics*, vol. 88, May 2006.

[16] D. Jenn, Notes for EC 3630 (Radiowave Propagation), Naval Postgraduate School, 2010 (unpublished).

[17] B.-K. Feng, “Extracting Material Constitutive Parameters From Scattering Parameters,” M.S. thesis, Naval Postgraduate School, Monterey, CA, 2006.

[18] W. Park and J. Kim, Guest Editors, “Negative Index Materials: Optics by Design,” *MRS Bulletin*, vol. 33, Oct. 2008.

[19] M. Dienerowitz, E. Mucciolo, L. Tkeshelashvili and K. Busch, “Theoretical Analysis of Negative Index Materials,” M.S. thesis, University of Central Florida, 2003.

[20] J.B. Pendry, D. Schurig and D. R. Smith,“Controlling Electromagnetic Fields,” *Science*, April 2006.

[21] Cotuk, Unit, “Scattering from Multi-layered Metamaterials Using Wave Matrices,” Naval Postgraduate School, Sep. 2005.

[22] David C. Jenn, *Radar and Laser Cross Section Engineering*, Second Edition, Ch. 7, pp. 335–388 , 2007.

[23] C. Caloz and T. Itoh, *Electromagnetics Metamaterials*, Wiley-Inter-Science, Hoboken, NJ, 2006.

[24] H. M. Musal, Jr., D. C. Smith, “Universal Design Chart for Specular Absorbers,” *IEEE Transactions on Magnetics*, vol. 26, no. 5, Sep. 1990.

[25] Cihangir Kemal Yuzcelik,” Radar Absorbing Material Design,” Naval Postgraduate School, Sep. 2003.

[26] G. T. Ruck, D. E. Barrick, W. D. Stuart, and C. K. Krichbaum, *Radar Cross* Section, Vol. 2, New York: Plenum Press, pp. 616–622, 1970.

[27] X. Chen, T. M. Grzegorczyk, B.I. Wu, J. Pacheco Jr., and J. A. Kong, “Robust Method to Retrieve the Constitutive Effective Parameters of Metamaterials,” *Phys. Rev. E.*, vol. 70, p. 016608, 2004.

[28] D. R. Smith, Wille J. Paddila, D. C. Vier, S. C. Nemat-Nasser and D. Schultz, "Composite Medium with Simultaneously Negative Permeability and Permittivity," *Physical Review Letters*, vol. 84, no. 18, May 2000.

[29] T. Weiland, R. Schuhmann, R. B. Greegor, C. G. Parazzoli, A. M. Vetter, D. R. Smith, D. C. Vier and S. Schultz, "Ab initio numerical simulation of left-handed metamaterials: Comparison of calculations and experiments," *Journal of Applied Physics*, vol. 90, no. 10, Nov. 2001.

[30] J. B. Pendry, A. J. Holden, D. J. Robbins and W. J. Stewart, "Magnetism from Conductors and Enhanced Nonlinear Phenomena," *IEEE Transactions on Microwave Theory and Techniques*, vol. 47, no 11, Nov. 1999.

THIS PAGE INTENTIONALLY LEFT BLANK

INITIAL DISTRIBUTION LIST

1. Defense Technical Information Center
   Ft. Belvoir, Virginia

2. Dudley Knox Library
   Naval Postgraduate School
   Monterey, California

3. Chairman
   Department of Physics
   Naval Postgraduate School
   Monterey, California

4. Chairman
   Department of Electrical Engineering
   Naval Postgraduate School
   Monterey, California

5. Professor David Jenn
   Department of Electrical and Computer Engineering
   Naval Postgraduate School
   Monterey, California

6. Professor Brett Borden
   Department of Physics
   Naval Postgraduate School
   Monterey, California

7. Professor James Luscombe
   Department of Physics
   Naval Postgraduate School
   Monterey, California

8. Embassy of Greece
   Office of Naval Attaché
   Washington, District of Columbia

9. LTJG Doumenis Christos
   Hellenic Navy General Staff
   Athens, Hellas (Greece)